

## Graphical Abstract

### **Terrain deformation measurements from optical satellite imagery: the MPIC-OPT processing services for geohazards monitoring**

Provost Floriane<sup>1</sup>, 2; Michéa David<sup>2</sup>, 3; Malet Jean-Philippe<sup>2,3,4</sup>; Boissier Enguerran<sup>5</sup>;  
Pointal Elisabeth<sup>6</sup>; Stumpf André<sup>7</sup>; Pacini Fabrizio<sup>5</sup>; Doin Marie-Pierre <sup>8</sup>;  
Lacroix Pascal<sup>8</sup>; Bally Philippe<sup>1</sup>

## Highlights

### **Terrain deformation measurements from optical satellite imagery: the MPIC-OPT processing services for geohazards monitoring**

Provost Floriane<sup>1</sup>, 2; Michéa David<sup>2, 3</sup>; Malet Jean-Philippe<sup>2,3,4</sup>; Boissier Enguerran<sup>5</sup>;  
Pointal Elisabeth<sup>6</sup>; Stumpf André<sup>7</sup>; Pacini Fabrizio<sup>5</sup>; Doin Marie-Pierre <sup>8</sup>;  
Lacroix Pascal<sup>8</sup>; Bally Philippe<sup>1</sup>

- Research highlight 1
- Research highlight 2

# Terrain deformation measurements from optical satellite imagery: the MPIC-OPT processing services for geohazards monitoring

Provost Floriane<sup>1, 2</sup>; Michéa David<sup>2, 3</sup>; Malet Jean-Philippe<sup>2,3,4</sup>; Boissier Enguerran<sup>5</sup>; Pointal Elisabeth<sup>6</sup>; Stumpf André<sup>7</sup>; Pacini Fabrizio<sup>5</sup>; Doin Marie-Pierre<sup>8</sup>; Lacroix Pascal<sup>8</sup>; Bally Philippe<sup>1</sup>

1. European Space Agency, ESA/ESRIN, Largo Galileo Galilei, 1, IT-00044 Frascati RM, Italy
2. Ecole et Observatoire des Sciences de la Terre, CNRS UAR 830 - Université de Strasbourg, 5 rue Descartes, F-67084 Strasbourg, France
3. Application Satellite Survey, A2S - CNRS/Université de Strasbourg, 5 rue Descartes, F-67084 Strasbourg, France
4. Institut Terre et Environnement de Strasbourg, CNRS UMR 7063 - Université de Strasbourg, 5 rue Descartes, F-67084 Strasbourg, France
5. Terradue, Via Giovanni Amendola, 46, IT-00185 Rome, Italy
6. ForM@Ter - Pôle de Données Terre Solide, Institut de Physique du Globe de Paris, Université Paris Diderot, 35 rue Brion, F-75013 Paris, France 7. GAF AG, Arnulfstraße 199, 80634 München, Germany
8. Institut des Sciences de la Terre, CNRS UMR 5275 - Université Grenoble-Alpes, 1381 rue de la Piscine, F-38610 Gières, France

---

## Abstract

Measuring terrain deformation over several spatial and temporal scales is relevant for many domains in Earth Sciences (i.e. co-seismic slip, volcanoes, landslides or glaciers monitoring). Optical and radar (SAR) satellite imagery is commonly used in the geophysical community. The development of optical satellite constellations covering the Earth with frequent revisit times at medium to high spatial resolutions is a major change allowing advanced time series analyses. The volume of data available represents also a chal-

lenght in terms of storage capacity and computing resources which, together with, the complexity of the processing (parameters tuning, combination of the image sequences, co-registration of the time series) may prevent users to exploit the data and extract relevant signals. We propose here a new version of the Multiple-Pairwise Image Correlation toolbox for processing OPTical images (MPIC-OPT); the toolbox provides a measurement of the sub-pixel displacement among one or multiple optical image pairs (sub-pixel image correlation) and is available as a service for automatic processing. The toolbox is based on image matching (MicMac open source library) and optical flow (GeFolKi open source library) techniques to track both small and large scale displacement. Several corrections (deramping, accross-track and along-track destripping) are available to increase the signal-to-noise ratio. Post-processing techniques (persistent motion detection, time series inversion) have been implemented to propose advanced products tailored to the user needs. The MPIC-OPT service has been deployed on the Tier 1.5 High-Performance Computing cluster (e.g. Datacentre/EOST-A2S) of the University of Strasbourg and is accessible through the ESA Geohazards Exploitation Platform (GEP) and/or the ForM@Ter Solid Earth computing infrastructure. Three MPIC-OPT services have been tailored according to requirements of the Earth science community: MPIC-SLIDE and MPIC-ICE designed respectively for the monitoring of landslides and glaciers using image time series, and MPIC-ETQ designed for the monitoring of co-seismic deformation triggered by large magnitude earthquakes from pairs of images.

MPIC-SLIDE and MPIC-ICE allow for advanced parameterization of the processing, while MPIC-ETQ is reduced in terms of number of parameters in order to increase accessibility of the service to a wide range of users. The services are currently tailored for Copernicus Sentinel-2; their performances are tested on several geohazard use cases, such as the monitoring of the Slumgullion landslide (USA) and the glaciers of the Mont-Blanc massif (Argentière / France) and the measurement of the co-seismic displacement of the 2019 Ridgecrest earthquakes (USA).

*Keywords:* Image Correlation; Time series analysis; Feature tracking; Time series inversion; Landslide deformation; Glacier deformation; Co-seismic displacement; Copernicus Sentinel-2; Geohazards Exploitation Platform (GEP); ForM@Ter

---

## <sup>1</sup> 1. Introduction

<sup>2</sup> Terrain motion is a parameter used in various field of Earth sciences for  
<sup>3</sup> understanding the physical mechanisms controlling volcano, fault, landslide  
<sup>4</sup> or ice glacier activity, but also for Disaster Risk Management (DRM). Several  
<sup>5</sup> techniques exist to measure the absolute or relative motion of the ground.  
<sup>6</sup> Some instruments can be installed in-situ (e.g. GNSS, extensometers) or  
<sup>7</sup> at proximity of the object of interest (e.g. terrestrial laser scanning, total  
<sup>8</sup> station) but the installation and maintenance of such instrumentation may be  
<sup>9</sup> challenging in inaccessible and remote areas. Conversely, space-borne sensing  
<sup>10</sup> of the Earth surface provides a global coverage and allow measurement over

11 extended areas (ca. 100kms<sup>2</sup>). The growing interest for these measures have  
12 lead to the development of numerous satellite constellations. In particular,  
13 several image time series of medium spatial resolution are publicly available  
14 such as the Copernicus Sentinels (since 2015 - (Gascon et al., 2017; Geudtner  
15 et al., 2014)) and the NASA long archive of the Landsat missions (since 1970  
16 - (Wulder et al., 2016)).

17 Terrain motion can be measured from space-borne observations using  
18 Radar (SAR) and Optical imagery. The two main techniques used in Earth  
19 Sciences are: a) Radar Interferometry (InSAR; (Gens and VAN GENDEREN,  
20 1996; Massonnet and Feigl, 1998)) and optical/SAR feature tracking; (Michel  
21 et al., 1999; Leprince et al., 2007)). Radar interferometry (InSAR) provides  
22 a measure of the ground motion at millimetric accuracy in the Line-of-Sight  
23 of the satellite by computing the phase difference between two acquisitions.  
24 Several approaches exist (D-InSAR, (Massonnet and Feigl, 1998); PSI, (Fer-  
25 retti et al., 2001; Hooper et al., 2004); PS/DS, (Ferretti et al., 2011)) and  
26 despite the complexity of the processing, they are widely used in different  
27 domains such as seismic source inversion (Massonnet et al., 1993; Wright  
28 et al., 1999) , volcano monitoring (Massonnet and Feigl, 1998; Hooper et al.,  
29 2004) or landslide detection (Hilley et al., 2004; Lauknes et al., 2010; Schlögel  
30 et al., 2015). However, InSAR presents some limitations, in particular for  
31 the monitoring of rapid terrain motion (e.g. velocity fields  $\gtrsim 1 \text{ m.yr}^{-1}$ ) due  
32 to a loss of phase coherence. Further, ground motion is measured in the  
33 satellite Line-of-sight (LOS) which prevents an easy interpretation of the

measure and limits the monitoring of movement in the azimuthal direction of the satellite. Conversely, image matching techniques can measure surface motion up to several pixels in the plane perpendicular to the satellite Line-of-Sight (LOS) and the technique can be applied to both SAR and optical images. In practice, the technique is mostly sensitive to motion in the horizontal plane in the North-South/East-West directions for most of the optical sensors or Azimuth/range directions for radar sensor. Vertical motion can be computed due to the viewing angle of the SAR sensor or by estimating the ortho-rectification bias for optical images with low off-nadir angles (Altena et al., 2019). The main limitations for using image matching techniques are due to errors in the image ortho-rectification, both for SAR radar and optical data, mostly in mountainous areas (Scherler et al., 2008). In the recent years, both techniques (InSAR and image matching) have started to be used jointly to retrieve the 3D displacements of several geological processes and for several kinematic regimes. The techniques have been used for the inversion of seismic sources (Konca et al., 2010; Scott et al., 2019; Bacques et al., 2020) where the co-seismic horizontal displacement are large (a few meters) near the fault and small at far distance from the fault. The two techniques are also commonly combined for monitoring glaciers at regional scales (Strozzi et al., 2004; Joughin et al., 2010; Dehecq et al., 2015).

Two main approaches exist to compute the offsets between pair(s) of images: a) the image matching approach that computes a similarity function over a sliding window to determine the new position of an object and b) the

optical flow approach that consists in retrieving the object motion by solving the brightness consistency equation for the whole image (Brigot et al., 2016). The main difference between the two approaches is the level of the results: sparse (i.e. feature-based) for image matching and dense (i.e. pixel-based) for optical flow. Image matching was first tested on satellite data in the early 1990's for the monitoring of ice glaciers (Bindschadler and Scambos, 1991; Scambos et al., 1992). The approach consists in measuring the similarity between the images based on the pixel intensity and the use of similarity functions (CC: Cross-Correlation; NCC: Normalized Cross-Correlation) calculated in the spatial or in the frequency (Fourier) domains ((Heid and Käab, 2012). Numerous algorithms have been developed such as ImCORR (Fahnestock et al., 1992), ImGRAFT (Messerli and Grinsted, 2015), COSI-Corr (Avouac et al., 2006), CIAS (Käab and Vollmer, 2000), MicMac (Rosu et al., 2015; Rupnik et al., 2017), and QPEC/Medicis (Cournet et al., 2016). These algorithms differ on their pre- and post-processing options. For example, ImCORR proposes a high-pass and low-pass filtering of the image as well as a Principal Component Analysis to reduce the satellite images features (Fahnestock et al., 2016) while MicMac proposes a regularization function to reduce outliers (Rosu et al., 2015). Optical Flow approaches have also been developed since the 1980's (Horn and Schunck, 1981) and applied to satellite observations for various applications like image co-registration (Brigot et al., 2016) or ice flow motion (Vogel et al., 2012; Altena and Käab, 2017; Lenzano et al., 2018). The formulation of the optical flow problem allows

for an estimation of less rigid motion fields at the pixel level. However, this approach is currently less used by the geoscience community compared to the image matching approach. The main limitations of optical flow remain on its sensitivity to strong changes in the images that prevents the technique to retrieve the motion associated to large displacement or to images with strong illumination differences (e.g. winter vs. summer acquisitions) (?). The optical flow approach hence becomes promising with short revisit time as is the case for recent satellite constellations (Altena and Käab, 2017) such as the Copernicus Sentinel-2 or the Planets Dove. Only few studies have compared the different approaches, and most of the comparison were carried out for ice glacier motion estimation (Heid and Käab, 2012; Millan et al., 2019), earthquake co-seismic motion (Rosu et al., 2015) and landslide motion (Le Bivic et al., 2017). The performance of the methods depend on the geological processes and thus the deformation type: (Rosu et al., 2015; ?) find that MicMac produces accurate results at a higher spatial resolution and with less outliers than COSI-Corr while (Heid and Käab, 2012) concludes that COSI-Corr in the frequency domain is well suited for ice flow motion. Recent implementations propose hybrid solutions taking advantages of both techniques (Brox et al., 2009; Weinzaepfel et al., 2013). The choice of the matching algorithm is crucial and testing several approaches is necessary for increasing reliability. As the many available solution are released in different processing environments (i.e. GUI, Graphical User Interface vs. CLI, Command Line Interface), it renders certain techniques more accessible to

others. Moreover with the current increase of the number of optical images available, post-processing is necessary to exploit the information contained in the stack of ground motion. (Stumpf et al., 2017) initiated the development of an end-to-end image matching workflow called Multiple-Pairwise Image Correlation (MPIC) which automatizes all the steps 1) from the query and download of the image dataset, 2) to the processing of multiple pairs of images and the creation of displacement grids, and 3) to the production of advanced information such as the retrieval of the mean velocity or the vector coherence from large stacks of displacement grids. Other toolboxes were developed since this initial work (Nagy et al., 2019; Millan et al., 2019; Van Wyk de Vries and Wickert, 2020; Ali et al., 2020).

The objective of this work is to present the new modular version of the MPIC-OPT workflow fully tailored for Sentinel-2 images, with several processing and advanced parameterization options, and optimized for high performance computing. MPIC-OPT is now organized in three modules: 1) the correlation module, 2) the correction and filtering module and 3) the spatio-temporal analysis module. In the first module, the correlation and the raw displacement fields are computed for each of the image pairs defined by the user. The new version of the service allows the creation of up to thousands of image pairs and the user can choose among an image correlator (MicMac; (Rupnik et al., 2017)) or an optical flow (GeFolKi; (Brigot et al., 2016)) approach. In the second module, the raw displacement field are corrected from geometric translation within the whole Sentinel-2 tile and within

126 each of the CCD imaging stripes(Stumpf et al., 2018). A new correction  
127 of jitter undulations of Sentinel-2, based on wavelet filtering of the horizon-  
128 tal features of the displacement fields, is presented. Several post-processing  
129 options are proposed to the users to filter the displacement fields (e.g. fil-  
130 tering of the largest displacement, filtering of the displacement across the  
131 slope direction, etc.). The third module aims at extracting spatio-temporal  
132 information from large stacks of ground motion grids. It is divided in two  
133 sub-functions: a) a multi-temporal fusion function to combine the pairs in  
134 order to retrieve spatial information (e.g. mean velocity, mean magnitude,  
135 etc.) and detect persistent ground motion, b) an inversion function to com-  
136 pute the motion time series which is on the Times-series Inversion for Optical  
137 images (TIO) algorithm (Bontemps et al., 2018; Doin et al., 2011). In order  
138 to tailor the services to science community applications and to allow opti-  
139 mized parameterization of the processing workflow, three thematic services  
140 have been designed: a) co-seismic displacement measurements with MPIC-  
141 OPT-ETQ; b) ice velocity monitoring with MPIC-OPT-ICE and c) landslide  
142 velocity monitoring with MPIC-OPT-SLIDE. The webservices are accessible  
143 online through the ESA Geohazards Exploitation Platform (GEP) and the  
144 ForM@Ter Solid Earth computing infrastructure. There performances are  
145 tested for three terrain motion use cases: i) the co-seismic displacement of  
146 the 2019 Ridgecrest earthquake sequence (USA), ii) the velocity monitoring  
147 of ice glaciers in the Mont-Blanc massif, and iii) the displacement monitor-  
148 ing of the Slumgullion landslide (USA). Each of the use case illustrates one

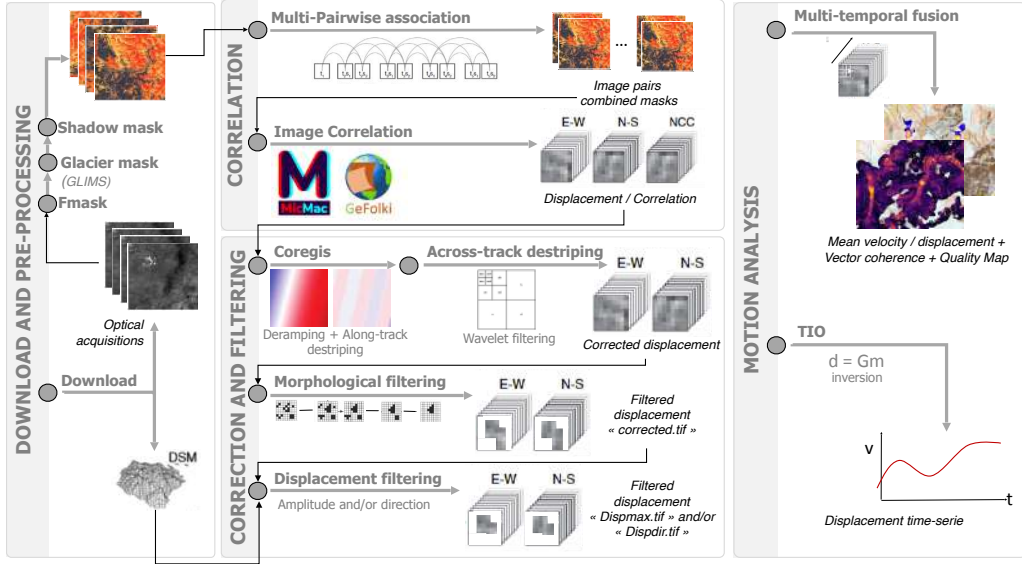


Figure 1: MPIC diagram.

of the newly integrated functions of the services. The MPIC-OPT derived displacement/velocity fields are compared to field measurements and other works recently published. The performances of the MPIC-OPT workflow are discussed as well as the choice of the parameters open for each service.

## 2. Description of the MPIC-OPT workflow

The MPIC-OPT workflow is organized in three modules (Figure 1). The first module allows correlating the image pairs, the second module allows for the correction and filtering of the displacement fields, and the third module allows to extract persistent motion from the stack of ground motion grids and the inversion of the time series. The modules are described in the following sections.

160 *2.1. Module 1: Image matching for quantifying ground motion*

161 Module 1 targets the computation of the offset shifts for each image pair.

162 In order to reduce the computation time, the images are first masked to re-

163 move the areas covered by clouds, water and snow (optional). The Fmask

164 algorithm (Qiu et al., 2019) is used to classify the pixels of the scene into

165 five categories (clear-view, water, cloud, cloud shadow and snow pixels). The

166 pairing of images is created by selecting a minimal and maximal matching

167 value in days or acquisitions. There is also an option to create the pairs

168 in both the direction of time ("Forward") and the reverse direction of time

169 ("Backward"). This can be used to improve the accuracy of the results by

170 increasing the Signal-to-Noise Ratio (SNR) (Stumpf et al., 2018). A split-

171 date can be set by the user to enable only the pairing of pre- and post-event

172 images (e.g. excluding the pairing of two pre- or post-event images). This op-

173 tion is designed particularly for co-seismic deformation analysis to increase

174 the Signal-to-Noise Ratio (SNR) by only computing the co-seismic pairs.

175 Once the pairing scheme is designed, two algorithms are available to com-

176 pute the offset shift for each of the pairs: MicMac (Rupnik et al., 2017) and

177 GeFolki (Brigot et al., 2016). MicMac is an open-source photogrammetric

178 library developed by IGN (Institut National de l'Information Géographique

179 et Forestière, France). The image matching function (Rosu et al., 2015;

180 Le Bivic et al., 2017) is a correlator in the spatial domain. The function

181 computes a correlation coefficient on a sliding window and proposes a reg-

182 ularization to stabilize the results especially for small windows sizes (Rosu

<sup>183</sup> et al., 2015). The main parameters exposed to the users in the service are  
<sup>184</sup> the sliding window, the spatial range, the regularization parameter and the  
<sup>185</sup> correlation threshold. The sliding window controls the amount of details of  
<sup>186</sup> the computed displacement (e.g. a small window allows to retrieve more de-  
<sup>187</sup> tails of the displacement field but may also be more affected by noise). The  
<sup>188</sup> spatial range corresponds to the expected maximum displacement and con-  
<sup>189</sup> trols the size of the search area to be matched with the sliding window. The  
<sup>190</sup> regularization parameter controls the smoothness of the final results (e.g.  
<sup>191</sup> a high regularisation parameter provides smooth displacement fields with a  
<sup>192</sup> low number of outliers). Indeed, a high regularization can reduce spatial  
<sup>193</sup> gradient of small-scale patches of displacement and hence mask their pres-  
<sup>194</sup> ence. This parameter is highly sensitive and must be chosen carefully. The  
<sup>195</sup> correlation threshold is used to reduce the computation time of the image  
<sup>196</sup> correlation, and is also used in the next steps of MPIC. GeFolki is a non-  
<sup>197</sup> parametric optical flow toolbox developed by ONERA (French Aeronautics,  
<sup>198</sup> Space and Defense Research lab). The main parameters exposed to the users  
<sup>199</sup> in the service are the radius, the number or levels, the number of iteration  
<sup>200</sup> and the rank. The radius defines the window size on which the matching  
<sup>201</sup> between the two images will be maximized. In practice, several radius are  
<sup>202</sup> defined as a power of two in order to increase the robustness of the estimation  
<sup>203</sup> (Brigot et al., 2016). The number of levels defines the number of layers in the  
<sup>204</sup> scale-pyramid which corresponds to different levels of down-sampling of the  
<sup>205</sup> images. The matching function is hence optimized iteratively for each levels

206 from the coarser to the finer one taking into account the shift estimation of  
207 the precedent level. Because the matching function in the case of optical flow  
208 is not linear, several iterations can be needed to approximate the solution.  
209 This number of iterations can be set by the user of the MPIC services. Fi-  
210 nally, several filters are applied to the input images to ensure that the images  
211 are similar enough to validate the brightness constancy model (Brigot et al.,  
212 2016). Among these filters, a rank filter is applied and the rank parameter  
213 defines the window size on which the values will be filtered.

214 The outputs of both algorithms consist in two offset grids in the horizontal  
215 plane (N-S, E-W). For MicMac, a third grid is calculated corresponding to a  
216 spatial distribution of the correlation coefficients .

217 *2.2. Module 2: Correction and filtering of ground motion*

218 Module 2 targets the correction and filtering of several sources of errors  
219 related to image geometry, image spectral properties and image matching.

220 *2.2.1. Deramping and destriping in the along-track direction*

221 Several sources of errors are recognizable in the raw displacement fields.  
222 First, rotational and translational shifts are observed between the input im-  
223 ages and result from coregistration errors of the Sentinel-2 (L1C) data. These  
224 shifts could be corrected by accurately reprocessing the raw images (Ding  
225 et al., 2016). However neither the Sentinel-2 raw data (L1B) nor the orbital  
226 positions of the satellites are available publicly. Post-processing corrections  
227 can be considered to model and correct these shifts, either as a linear ramp

228 (Bontemps et al., 2018) or as a plane (Stumpf et al., 2018; Ding et al., 2016):

$$\Delta x_{m,i} = a_x + b_x x_{r,i} + c_x y_{r,i}$$

$$\Delta y_{m,i} = a_y + b_y x_{r,i} + c_y y_{r,i}$$

229 where  $x_{m,i}$  and  $y_{m,i}$  are the modelled offset and  $x_{r,i}$ ,  $y_{r,i}$  are the spatial  
230 coordinates of the  $i^{th}$  pixel in the displacement fields. The coefficient of these  
231 planes  $a_{x/y}$ ,  $b_{x/y}$ ,  $c_{x/y}$  are estimated by an iteratively reweighted least square  
232 (IRLS) with a bi-square loss function minimizing the residuals between the  
233 measured and modelled offsets ((Stumpf et al., 2018)). The estimated planes  
234 are then removed from the raw displacement grids.

235 Second, in Sentinel-2 acquisitions, regular stripe artifacts are visible along  
236 the track direction in most of the displacement fields. This is due to the struc-  
237 ture the image which includes 12 pushbroom sensors that scan the ground  
238 along different tracks. Consequently, shifts and overlaps are reported for all  
239 satellite with embedded pushbroom sensors like Sentinel-2 (Stumpf et al.,  
240 2018; ?) but also for Landsat-8 (Ding et al., 2016) and Spot-4 (Ayoub et al.,  
241 2008). In order to correct these effect, (Leprince et al., 2008) proposes a  
242 pre-processing approach to model and calibrate the CCD shifts as a posi-  
243 tionning error of each CCD sensors. For Spot-4 images, the results show  
244 that the CCD shifts can be reduced by one order of magnitude (Leprince  
245 et al., 2008). However, this procedure includes a precise coregistration and

246 orthorectification which implies the availability of a reference image with no  
247 geometric errors, an accurate DEM and the orbital information (Leprince  
248 et al., 2008). The former are not available for Sentinel-2 preventing to ac-  
249 curately model this effect in a pre-processing strategy. (Stumpf et al., 2018)  
250 proposes a post-processing methodology to correct the CCD shifts from the  
251 displacement fields. The mean shift is estimated within each CCD tracks  
252 (which footprints are provided in the Sentinel-2 metadata) and subtracted.  
253 This strategy is the one implemented in the MPIC-OPT services.

254 *2.2.2. Destripping and jitter vibration correction in the across-track direction  
255 using wavelet filtering*

256 In some cases, regular across-track undulations are visible in the dis-  
257 placement fields. These stripes are usually due to attitude jitter undulation  
258 which refer to sensor vibrations due to on-board dynamics of the pushbroom  
259 sensors or to external perturbations causing attitude variations. The jit-  
260 ter undulations manifest in the across-track direction at different magnitude  
261 and frequency depending on the satellites (Ayoub et al., 2008; Teshima and  
262 Iwasaki, 2008; Kääb et al., 2016; Nagy et al., 2019; Ye et al., 2019). As jitter  
263 undulation is present within each acquisition and their combination (e.g. im-  
264 age correlation) can be constructive or destructive (Kääb et al., 2016). The  
265 magnitude of the jitter undulation may be as large as 16 meters for Sentinel-2  
266 images (Nagy et al., 2019) and hence, may be an important source of noise  
267 for ground motion analysis. Several approaches can be used to correct this

source of noise: COSI-Corr (Avouac et al., 2006) proposes to accurately or-  
thorectify the slave image taking into account the attitude information of  
the sensor (Scherler et al., 2008). However, if the sampling frequency of the  
attitude is too low with respect to the acquisition frequency, the modelling of  
the orbital trajectory will not allow correcting the jitter undulation (Teshima  
and Iwasaki, 2008). Moreover, in the case of Sentinel-2, the Level-0 images  
and orbital information are not available which prevents to apply the appli-  
cation of this approach (Wang and Bürgmann, 2020). Other strategies have  
been proposed and the most common ones consist in computing the average  
of the displacement in the across-track direction (Scherler et al., 2008) and  
remove it along the across-track direction. However, these corrections needs  
a careful control of the user to ensure the jitter undulations are estimated  
over stable areas and does not deteriorate the under-laying ground motion  
(e.g. co-seismic displacement).

The problem of removing stripes within an image is addressed in other  
scientific domain such as medical imagery for noise filtering (Renier et al.,  
2016; Kirst et al., 2020). A common solution is to use wavelet filtering to re-  
move undulations of a certain frequency and orientation. The python library  
*pystripe* was initially developed to remove streaks on selective/single plane  
illumination microscopy images (Kirst et al., 2020). This library was adapted  
for filtering the jitter undulation of the Sentinel-2 images. The method con-  
sists in applying a discrete wavelet decomposition of the image that returns a  
coarse approximation of the original image and wavelet coefficient called *de-*

*tail coefficients.* The details coefficients correspond to the high-pass content of the image in the horizontal, vertical and diagonal directions that has been removed from the coarse approximation of the image. The decomposition is repeated recursively on the approximation image. The jitter undulations are present mainly in the horizontal detail coefficients. A threshold is applied on the horizontal coefficient to filter out the horizontal detail coefficients. The image is then reconstructed with the function *waverec2*. The choice of the wavelet is critical for the stripe removal. Among the large range of wavelet families available, the Daubechies wavelet family was chosen for this correction. The first ten Daubechies wavelets have been tested on a synthetic signal simulating a mixture of a synthetic fault-like signal and a real jitter signal from the Sentinel-2 pairs A trade-off is observed between the removal of the jitter noise and the deterioration of the fault motion in particular at proximity of the fault. From many simulations, we determined that the Daubechies ('db5') is the most suitable wavelet to remove jitter undulations in Sentinel-2 images without destroying near-fault displacement.

### *2.2.3. Topographic and morphological filtering*

Additional topographic and morphological filters are proposed for the monitoring of landslides and glaciers. These filters rely on the assumption that such processes occur along the slope with a rheology that leads to spatially coherent and smooth motion fields in terms of motion direction and amplitude (Stumpf et al., 2017). The main objective of this filter is hence

313 to filter out the patches of motion that are incoherent with this assumption.  
314 First, a morphological filter is applied by default to remove small isolated  
315 motion patches. Second, the displacement fields are filtered with respect  
316 to the slope aspect and the slope angle. The user can filter out a certain  
317 range of slope angles depending on its application. For instance, flat regions  
318 ( $\theta < 5$ ) can be filtered out for monitoring landslides in mountainous areas  
319 while steep regions ( $\theta > 30$ ) can be filtered out (in certain cases) when study-  
320 ing co-seismic displacement to reduce the effects of DEM errors (Kääb et al.,  
321 2016). Moreover, the user can decide to filter the motion field according to  
322 the direction of the slope assuming the motion occurs downward the slope  
323 direction. The maximum angle allowed between the slope direction must  
324 be chosen carefully to filter erroneous displacement vectors without filtering  
325 motion of interest. Two global DEM are currently available to apply the  
326 filtering: the MERIT-DEM at 90m resolution (Yamazaki et al., 2017) and  
327 the Copernicus DSM at 30m resolution (cop).

328 *2.3. Module 3: post-processing of ground motion for geophysical information  
329 retrieval*

330 Module 3 provides a series of post-processing analysis tools in order to  
331 retrieve geophysical information from the displacement fields. The first part  
332 of the module estimates the mean displacement and velocity over the period  
333 investigated as well as the coherence of the displacement vector which is a  
334 good indicator of the area in motion (Stumpf et al., 2017). The second part

335 of the module provides an inversion of the time series of the displacement for  
336 each pixel and for each direction (NS, EW) over the period investigated.

337 *2.3.1. Multi-temporal fusion module*

338 Multi-temporal fusion consists in summarizing the information contained  
339 in the stack of the computed displacement fields. This tool was developed in  
340 the previous version of MPIC and is described in (Stumpf et al., 2017). The  
341 main indicator of movement consists in computing the mean velocity over the  
342 stack of displacement. The robustness of this indicator to detect areas in mo-  
343 tion depends on the kinematic behavior of the object of interest and the time  
344 interval considered to build the image pairs. Indeed the arithmetic mean is  
345 particularly suitable in the case the motion is constant over time regardless of  
346 the considered time interval between the pairs of images. However, seasonal  
347 periods of acceleration and deceleration are commonly observed on glaciers  
348 and landslides (Coe et al., 2003; Stumpf et al., 2017; Altena and Kääb, 2017;  
349 Millan et al., 2019) and in that case, the choice of the time interval is critical  
350 for the meaning of the mean velocity. Indeed, the long-term mean veloc-  
351 ity of glacier can be estimated by setting long time interval ( $> 1\text{year}$ ) to  
352 create pairs of images over a long archive of images (Dehecq et al., 2015).  
353 Conversely, zones of rapid acceleration can be detected by reducing the time  
354 interval. The second feature computed by the multi-temporal fusion tool is  
355 the vector coherence that estimates the coherence of the motion direction  
356 over time. A vector coherence ranges from 0 to 1 with a vector coherence

357 of 1 meaning that the motion occurs along the exact same direction over  
358 time (Stumpf et al., 2017; Dehecq et al., 2015). Vector coherence has been  
359 demonstrated to be a relevant indicator to detect unstable areas (Stumpf  
360 et al., 2017) over wide territories ( $10\text{km}^2$ ).

361 *2.3.2. Time-series inversion module*

Stacks of displacement fields (NS, EW) can be inverted to retrieve the displacement time series for each pixel of interest. The tool is based on the Time-Series Inversion for Optical images algorithm (Bontemps et al., 2018) initially developed for interferogram time series (Doin et al., 2011). Considering N optical images, it is possible to create  $M < N(N - 1)$  pairs. The inversion consists in solving the system of equation for the pixel i:

$$d_i = G\lambda_i \quad (1)$$

362 where  $d_i$  corresponds to the displacement fields computed in module 1 and  
363  $\lambda_i$  corresponds to the incremental displacement to be inverted. G is a MxN  
364 matrix containing 0 and 1 depending on the network of pairs set up by the  
365 uset.

Weights are chosen to improve the Signal-to-Noise Ratio (SNR) by attributing larger contribution for certain displacement fields compared to other considered as less robust. (Lacroix et al., 2019) proposed to weight the pairs with respect to their temporal baseline ( $\Delta T$ ) giving a larger weight to pairs with short baseline assuming less decorrelation. However, it might be

considered that in the case of slow motion and if the sensitivity of the image matching algorithm is  $1/10^{th}$  of pixel, short pairs may not retrieve correctly the displacement. For example if the motion is 1m/year and is monitored by Sentinel-2 acquisitions (10x10m pixel), the image matching algorithm will be sensitive to the motion for pairs of one year or more. To take in consideration this case, we propose two different weighting function to the user:

$$w_l^{short} = \frac{1}{1 + (\Delta T_l - \Delta T_{min})} \quad (2)$$

$$w_l^{long} = \frac{1}{1 + (\Delta T_{max} - \Delta T_l)} \quad (3)$$

where  $w_l^{short}$  is a weighting function that gives larger weights to pairs with short temporal baselines while  $w_l^{long}$  gives larger weights to long temporal baselines.  $T_l$ ,  $T_{min}$  and  $T_{max}$  are, respectively, the temporal baselines of the pair  $l$ , the minimal and the maximal matching range.

The system of equations 1 is solved by a least-square inversion and in case of rank deficiency with a Singular Value Decomposition (López-Quiroz et al., 2009). Rank deficiency occur when the group of images cannot be linked to another which prevents for the inversion of the system. By default, two iterations are realized including the re-weighting scheme with the network misclosure (Bontemps et al., 2018). The network misclosure  $R_i = d_i - G\lambda_i$  is the difference between the displacement fields ( $d_i$ ) and the estimated displacement fields after inversion of the incremental displacement ( $\lambda_i$ ). High values of network misclosure usually indicate inverted displacement with large bi-

ases and likely wrong estimation of the displacement. In order to minimize the influence of these pairs in the second iteration, an additional weight is considered:

$$W_i^j = w_i^* \frac{1}{R_0^2 + R_i^{j2}} \quad (4)$$

where  $R_0$  is a constant that must be approximately equal to the noise standard deviation (Bontemps et al., 2018) and  $R_i^j$  is the network misclosure for pixel j and pair i.

The inversion procedure is applied independently to the set of NS and EW displacement pairs. The outputs of the tool provide the incremental displacement values at each acquisition date, the mean velocity and the Root Mean Square Error (RMSE) of the displacement estimation for each inverted value.

### 3. Performance of MPIC-OPT for co-seismic, landslide and glacier motion analysis

#### 3.1. Co-seismic motion triggered by the July 2019 Ridgecrest earthquake sequence

In July 2019, several thousands of earthquake were recorded in Southern California near the town of Ridgecrest close to the Eastern California Shear Zone (ECSZ), the Little Lake Fault zone (LLFZ) and at the East of the San Andreas Fault System (SAF) (Chen et al., 2020; Ross et al., 2019). Two main earthquake events occurred on July 4 and July 6, 2019

387 (UTC) with magnitudes of Mw 6.4 and Mw 7.1 respectively revealing a  
388 complex fault system (Figure 2). Indeed, these two events activated two  
389 conjugate faults oriented northwest–southeast (right-lateral strike slip) and  
390 northeast–southwest(left-lateral strike slip). The rupture reached the surface  
391 at different location and the fault system could be mapped from field obser-  
392 vations (DuRoss et al., 2020), from satellite interferogram analyses (Field-  
393 ing et al., 2020; Xu et al., 2020) and from satellite optical image analysis  
394 (Milliner and Donnellan, 2020). The field observations measured a horizon-  
395 tal offset of up to 5m on the northwest–southeast faults and 1.6m on the  
396 northeast–southwest fault (DuRoss et al., 2020). The focal mechanism of  
397 the ruptures and the magnitude of the horizontal motion make offset track-  
398 ing techniques particularly interesting to measure the co-seismic deformation  
399 in particular at proximity of the fault line. The technique has been applied  
400 on Sentinel-1 (Fielding et al., 2020; Ross et al., 2019) and Cosmo-Skymed  
401 SAR data (?) and on Planetlab (Milliner and Donnellan, 2020) and Sentinel-  
402 2 (Chen et al., 2020) satellite optical images. The MPIC-OPT-ETQ service  
403 has been applied on Sentinel-2 images. The obtained ground motion, and in  
404 particular, the effect of the jitter correction are discussed and compared to  
405 field observations and to other image correlation techniques applied on the  
406 same pair of images (Chen et al., 2020).

407 Two cloudless Sentinel-2 acquisitions acquired on June 28, 2019 and July  
408 8, 2019 before and after the occurrence of the two main ruptures are used.  
409 MPIC-OPT-ETQ runs were realized with the following parameterization. We

410 used the MicMac image matching library (Rupnik et al., 2017) on a window  
411 size of 5x5 pixels with a regularization coefficient of 0.3 and a matching range  
412 of 2. Deramping and along-track destriping correction were applied on the  
413 displacement field as described in section 2.2. The displacement fields are  
414 strongly affected by the Sentinel-2 CDD stripes and by sensor jitter undula-  
415 tions (Figure 2a, c). This dataset is thus an ideal use case for evaluating the  
416 operational performance of the jitter correction integrated in the MPIC-OPT  
417 services. The displacement fields corrected with the across-track destriping  
418 procedure (cf. section 2.2) are plotted in Figure 2b, d. The wavelet filtering  
419 allows to decrease the Root Mean Square Error (RMSE) of the North-South  
420 and East-West displacement fields by 15cm. The RMSE of the full Sentinel-2  
421 tile is thus ca. 0.35m ( $100km^2$ ). The jitter undulations are particularly visi-  
422 ble on the EW displacement field (Figure 2a) and are clearly removed after  
423 the correction (Figure ??,b and e) without loosing the displacement signal  
424 close to the fault. The CCD stripes remain visible because of undulations  
425 along the track direction within each CCD stripes. These undulations are  
426 difficult to remove automatically as their spatial wavelength is of the same  
427 magnitude as the one of the co-seismic motion.

428 The performance of MPIC-OPT-ETQ is further evaluated against other  
429 satellite-derived ground motion products (Chen et al., 2020) and field obser-  
430 vations. We computed the displacement for the same pair of images with a  
431 regularization parameter of 0.03 to allow for more spatial heterogeneity in  
432 the displacement fields in order to capture the displacement magnitude at

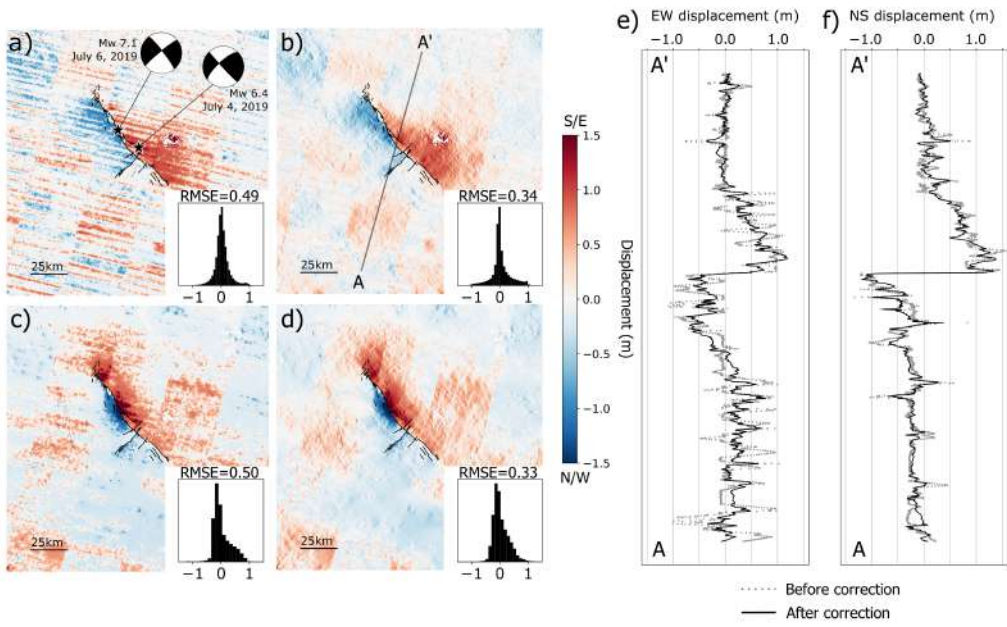


Figure 2: Effect of wavelet filtering on the NS and EW components of the Ridgecrest earthquake co-seismic displacement for a pair of Sentinel-2 images covering the period June 28 - July 10, 2020. The EW and NS components before the correction are plotted on subplots a) and c) respectively and after the correction on subplots b) and d). The displacement field is plotted along profile AA' for e) the EW and f) the NS component respectively.

the fault lines. The images were correlated in the forward and backward temporal direction to increase the SNR and the displacement fields were averaged. This operation was repeated for the Sentinel-2 bands 2, 3, 4 and 8 (i.e. red, green, blue and infra-red bands). The final displacement fields in NS and EW components are the average of the displacement fields for each band. The displacement magnitude is plotted on Figure ??,a. The results of (Chen et al., 2020) obtained with the Cosi-Corr algorithm are plotted on Figure 3d. The two displacement fields are in agreement for both the magnitude and direction (Figures 3 and refFig4c). However, the jitter undulations remain visible on the Cosi-Corr results on the Eastern part of the main fault (AA',Figure 3d) despite the large correlation window (32 x 32 pixels); the MPIC-OPT-ETQ results are less noisy and less contaminated by outliers (Figure 3 and 4c) due to the MicMac regularization function (Rosu et al., 2015; Le Bivic et al., 2017). Together with the jitter correction, the MPIC-OPT-ETQ results capture the co-seismic displacement at a much higher spatial resolution (25m against 150m for Cosi-Corr) allowing to map the relative displacement between the different blocks of the fault (zoomed area in Figure 3a and d). In particular, the displacement fields obtained with MPIC-OPT-ETQ show a homogeneous southeast direction within the block in the middle of the two most external faults (inset in Figure 3a) while the Cosi-Corr displacement fields indicate a localized southwest direction not coherent with the surrounding displacement direction (inset in Figure 3d).

To compare the field measurements with the ones obtained with Sentinel-2

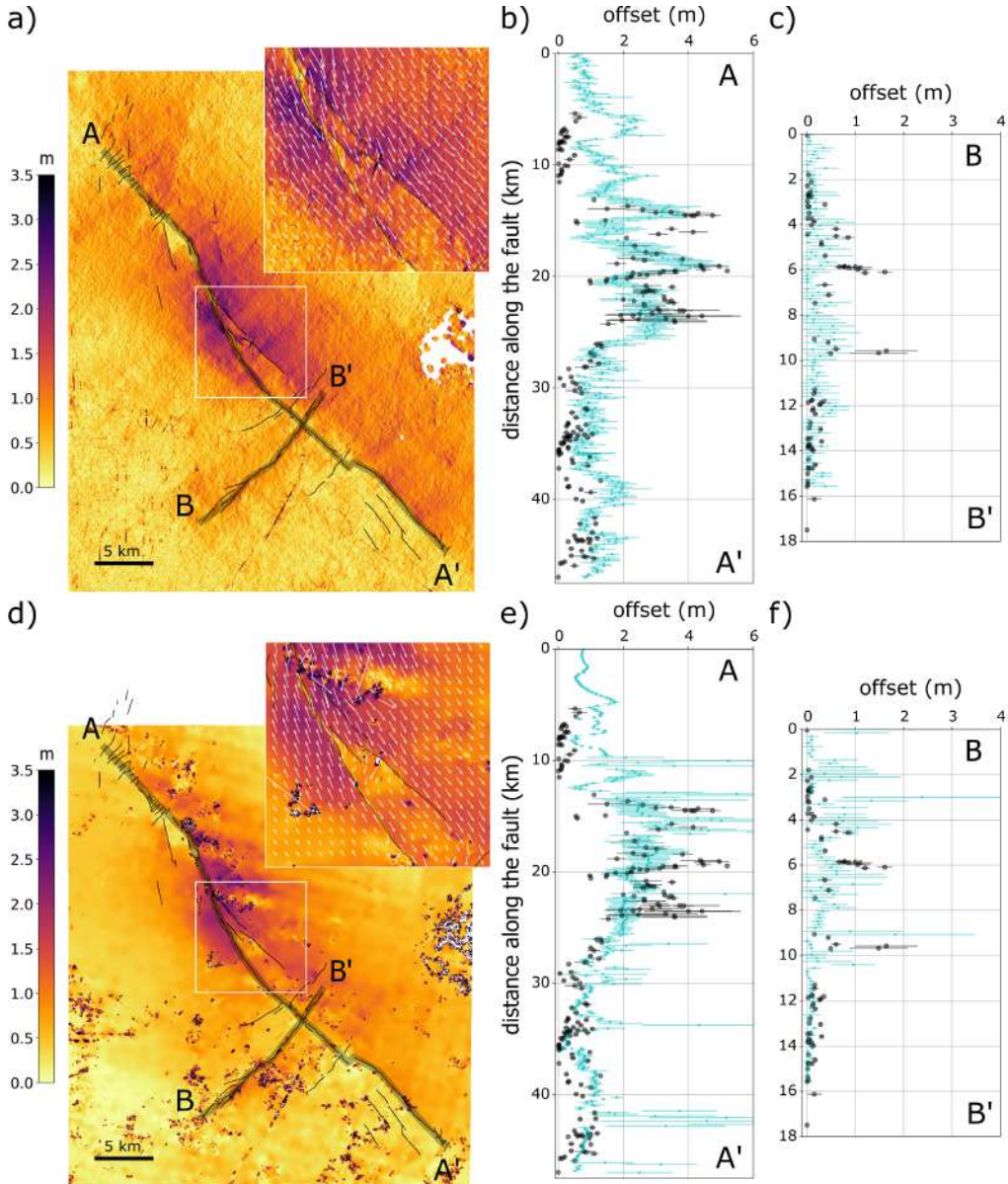


Figure 3: Comparison of the total displacement fields ( $\sqrt{d_{NS}^2 + d_{EW}^2}$ ) between June 28 and July 10, 2019 using MPIC-OPT-ETQ (top) and Cosi-Corr (bottom);(Chen et al., 2020)). a,d) Horizontal displacement magnitude; Horizontal offset at the fault for profile AA' (b,e) and BB' (b,e) with the measured offset from Sentinel-2 images (in blue) and the field observations (in black) (?).

456 image correlation, the geometry of the two main fault lines are simplified (Figure  
457 3,a,d; profiles A-A' and B-B'). Cross-sections are computed every 250m  
458 along the profile lines and the horizontal offsets at the fault are computed by  
459 averaging the displacements over 200m in the perpendicular direction to the  
460 fault line. The comparison between the field observations and the outputs of  
461 MPIC-OPT-ETQ is plotted on Figure 4a for MPIC-OPT-ETQ and on Figure  
462 4b for Cosi-Corr for the two main faults. Overall, the results are in agreement  
463 (Figure 4c). The MPIC-OPT-ETQ results show better agreement with the  
464 field measurements with a regression coefficient of 1.12 (Figure 4a) than the  
465 Cosi-Corr (regression coefficient of 0.49). This is explained by the fact that  
466 the Cosi-Corr displacement fields contained strong estimations (>5m) that  
467 are not confirmed by field observations (Figure 4b). On fault AA', the two  
468 products can discriminate the region with strong offsets and slightly overesti-  
469 mate the ground motion where field observations measure decimetric offsets  
470 (<1m). On fault BB', strong offsets (>1m) are observed in very localized  
471 areas (at 6 and 10km). The MPIC-OPT-ETQ results enable to map this  
472 localized deformation (Figure 3c) while the Cosi-Corr results map correctly  
473 the fault offset at 4 to 6km but also overestimate the displacement at several  
474 locations (Figure 3f).

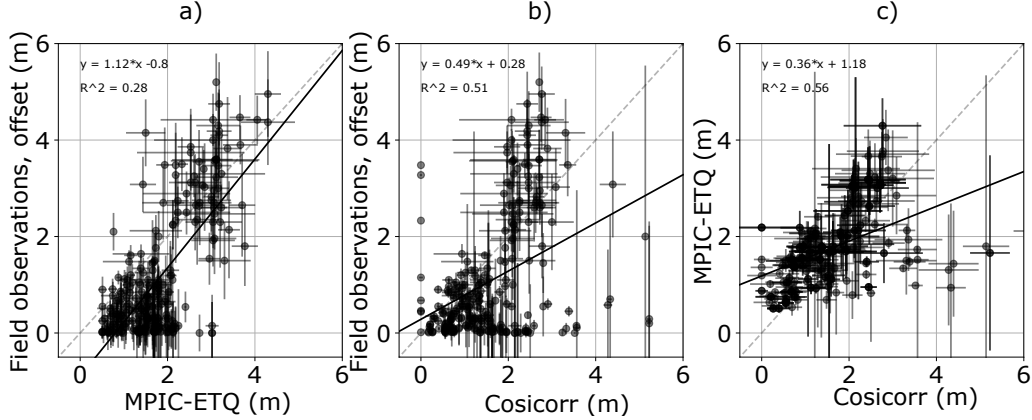


Figure 4: Comparison of Sentinel-2 derived motion (with MPIC-OPT-ETQ, Cosi-Corr) to field observations (?). The linear function  $y = x$  is plotted in grey (dotted line) and the result of the linear regression is plotted in black with the parameters of the regression indicated in the upper right corner.

475     3.2. Alpine glacier motion in the Mont-Blanc massif from Sentinel-2 image

476       time series

477     Several of the most active European alpine glaciers (Brenva, Bossons,  
 478     Mer de Glace and Argentière) are located in the Mont-Blanc massif (France,  
 479     Switzerland, Italy). A time series of Sentinel-2 images covering the period  
 480     July 2015 to June 2020 was selected with a cloud-coverage lower than 20%.  
 481     From this initial selection, a second selection was carried out by inspecting  
 482     the cloud coverage over the Region Of Interest (ROI). The MPIC-OPT-ICE  
 483     service is used with the MicMac correlator; the pairs were constructed for  
 484     time differences between two images lower than 100 days. This criteria was  
 485     defined to allow comparison with precedent studies (Dehecq et al., 2015;  
 486     Millan et al., 2019). The mean velocity for the whole period is plotted on  
 487     Figure 5. The ice velocity ranges from about  $50 \text{ m.year}^{-1}$  on the lower part

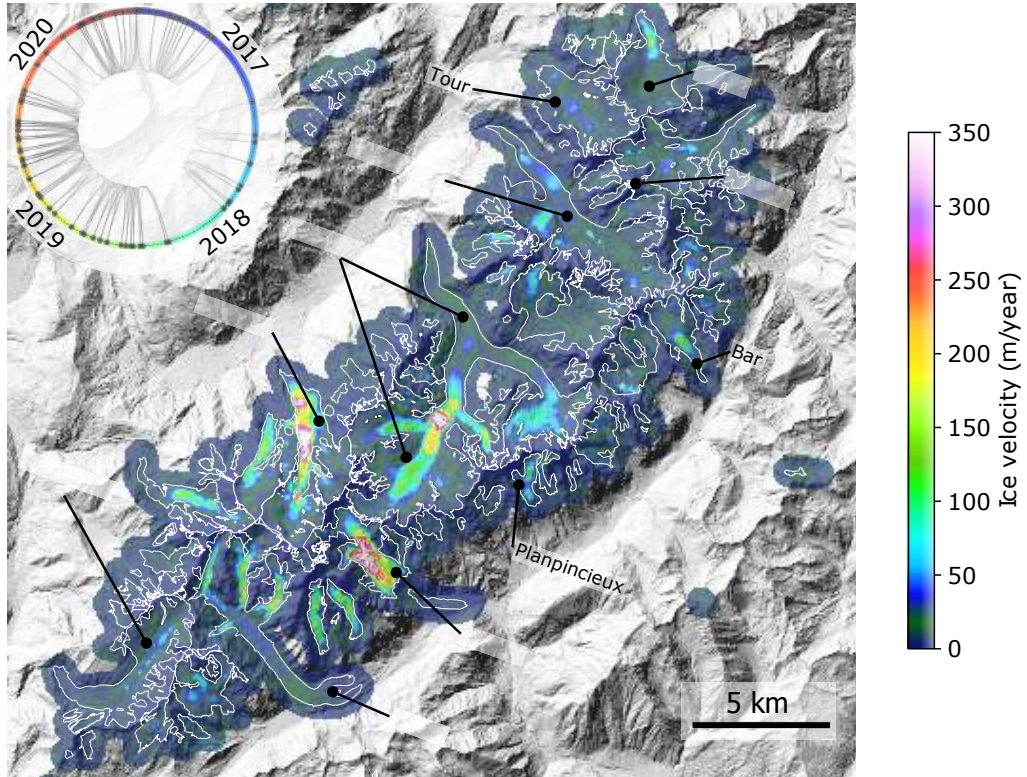


Figure 5: Results of MPIC-OPT-ICE on the Mont-Blanc (European Alps) alpine glaciers, expressed in mean surface velocity and in meters per year for the 2015-2020 period. The surface velocities are overlaid over the Copernicus 30m Digital Surface Model (DEM). The upper left diagram represents the pairing network between the 70 acquisitions used in the processing.

of the Argentière glacier to nearly  $350 \text{ m.year}^{-1}$  in the upper part of the Mer de Glace glacier. These velocities are in agreement with previous studies over the same area (Dehecq et al., 2015; Millan et al., 2019). Smaller active glaciers are also visible like the Planpincieux glacier.

The surface velocities measured with the MPIC-OPT-ICE service are compared to in-situ GNSS campaigns provided by the GlacioClim observatory (glacioclim.osug.fr). The GNSS velocity database consists in differential

495 measurements of targets placed at different locations on the Mer de Glace  
496 (10 to 17 targets per year) and Argentière (40 to 60 targets per year) glaciers.  
497 The measurements are taken two times per year in late summer/early fall.  
498 To compare the in-situ observations with the MPIC-OPT-ICE results, we  
499 divided the Sentinel-2 dataset into yearly subsets and recomputed the mean  
500 velocity (Figure ??). The results show a variability of the mean velocity for  
501 the 4 years. The periods 2016-2017 and 2017-2018 present more noisy re-  
502 sults; indeed the stable areas surrounding the glaciers show velocities larger  
503 than  $50 \text{ m.year}^{-1}$ . Conversely, in the period 2015-2016 and 2018-2019, the  
504 velocities over the stable areas are well resolved. This variability in the ve-  
505 locity estimation can not be explained by the number or the distribution of  
506 Sentinel-2 images over the year; it is more likely caused by the presence of  
507 fresh snow that may have prevented to track properly the motion.

508 Figure 6 shows the comparison between the MPIC-OPT-ICE and the  
509 GlacioClim ice velocity measurements. The Sentinel-2 mean velocity is com-  
510 puted as the mean of an area of  $3 \times 3$  pixels around the location of the target  
511 positions and the standard deviation is represented as error bars on Figure 6.  
512 For the Mer de Glace glacier (Figure ??a), the two sets of measurements are  
513 in agreement. MPIC-OPT-ICE tends to slightly underestimate the higher  
514 velocity ( $> 90 \text{ m.year}^{-1}$ ) by around  $20 \text{ m.year}^{-1}$ . Conversely, the results on  
515 the Argentière glacier are not in agreement. GlacioClim measures velocity  
516 ranging from 40 to  $60 \text{ m.year}^{-1}$  while MPIC-OPT-ICE is measuring on the  
517 same points velocities ranging from 25 to  $175 \text{ m.year}^{-1}$ . This bias is ob-

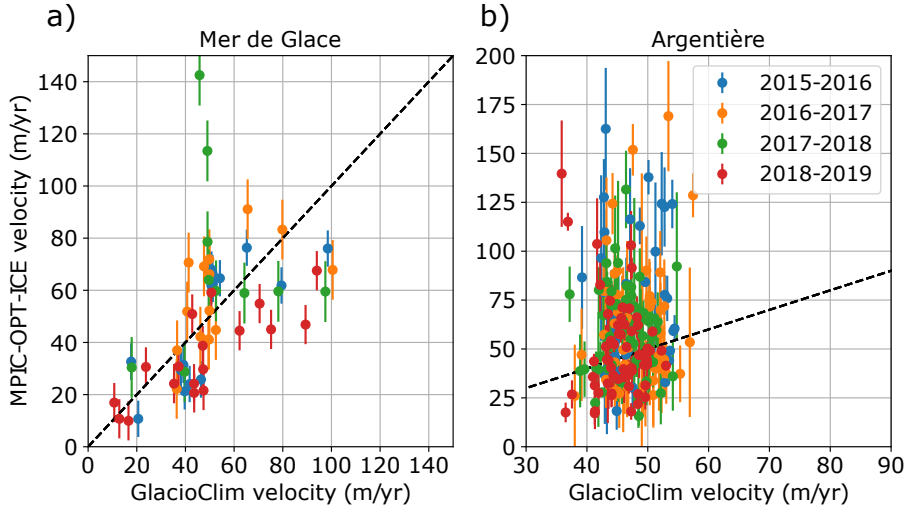


Figure 6: Comparison between the GlacioClim ([glacioclim.osug.fr](http://glacioclim.osug.fr)) and the MPIC-OPT-ICE ice velocity measurements for the Mer de Glace (a) and Argentière (b) glaciers.

served for every yearly subset. Similar inaccuracies have been noticed by (Millan et al., 2019) on the Argentière glacier when comparing the velocity from satellite observations and the ones measured by differential GNSS. The Argentière is located at much higher elevations (i.e. 2600 to 3100m) than the Mer de glace (< 2500m) resulting in earlier snow cover which prevents the measure of the ice motion for most of the pairs.

*3.3. Ground motion of the Slumgullion landslide from Sentinel-2 image time series*

The MPIC-OPT-SLIDE service is used to quantify the surface velocity of the Slumgullion landslide (Colorado, USA) which extends over a distance of 6.5 km for a width of 0.6 km and presents a translational motion (Schulz et al., 2009). The landslide has been widely studied and its motion is regu-

larly monitored with several instruments (extensometers, GB-InSAR (Schulz et al., 2012), UAVSAR (Hu et al., 2020)). The most active part of the land-slide creeps at a velocity of 1-2 cm.day<sup>-1</sup> (Fleming and , US; Coe et al., 2003; Schulz et al., 2012; Hu et al., 2020). This range of velocity is too rapid to be detected by medium-resolution Sentinel-1 (20 x 10 m) satellite radar interferometry (Hu et al., 2020) while it can be captured by higher resolution Cosmo-Skymed (5 x 3 m) SAR images (Milillo et al., 2014). SAR amplitude offset-tracking methods have been tested using spaceborne (e.g. Cosmo-Skymed (Amitrano et al., 2019), TerraSAR-X (Madson et al., 2019)) and airborne (e.g. USAVSAR (Delbridge et al., 2016; Hu et al., 2020)) acquisitions. However, these datasets consist of a limited number of acquisitions preventing to monitor the seasonal evolution of the slope. To our knowledge, archives of optical images have currently not been exploited to monitor the slope motion with the exception of Guerriero et al. (2020) who used Google Earth images.

MPIC-OPT-SLIDE is tested to define the capability of medium resolution Sentinel-2 (10 x 10m) optical data acquired at high frequency (every 5 days) to monitor slow-moving landslides. The archive from 2015 to 2020 offers 97 cloud-free images; the image pairs were created with a temporal baseline ranging from 500 days to 1500 days resulting in 853 pairs (Figure 7a). We compute the displacement grids with MicMac and GeFolki to compare the performance of the two algorithms. The displacement time series are inverted using the TIO algorithm. For the inversion, the pairs are not weighted in

553 function of their temporal baseline.

554 The mean velocity is computed from the stack of the displacement grids  
555 for MicMac (Figure 7b) and GeFolki (Figure 7c). The two results are in  
556 agreement with each other and detect the same active area located in the  
557 central part of the landslide with a mean velocity of ca.  $1.4 \text{ cm.day}^{-1}$ . Both  
558 the magnitude and the direction of the mean velocity vectors of the two algo-  
559 rithms are in agreement although the extension of the active zone is smaller  
560 with GeFolki due to lower velocity magnitude and spatially less coherent  
561 vectors (Figure ??c).

562 Figure 8a and b displays the comparison between in-situ measurements  
563 with extensometers and the displacement time series inverted with TIO from  
564 the stack of displacement computed with MicMac (Figure ??a) and GeFolki  
565 ((Figure ??b). The values of the displacement time series are plotted for the  
566 points surrounding the location of the extensometers (located at less than  
567 20 m) as well as their Root-Mean Square Error (RMSE). The comparison  
568 between the in-situ and the inverted data are possible only between June 2016  
569 (first cloudless acquisition of Sentinel-2) and October 2018 (last acquisition  
570 of the USGS extensometers. The results of MicMac (Figure 8a) and GeFolki  
571 (Figure 8b) are in agreement with each other for the three extensometer  
572 locations. However, the GeFolki time series are noisier and RMS errors are  
573 larger than the ones obtain with MicMac. The total cumulative displacement  
574 are slightly larger for GeFolki in comparison with MicMac in particular for  
575 point 1 in the central most active part of the landslide with a difference

of 2 m. Both methods show good agreement with the in-situ data (Figure 8a, b) except for point 1 for which the inversion tends to over-estimate the displacement for both GeFolki and MicMac dataset.

### 3.4. Sensor and algorithm precision

We use the methodology described in (Millan et al., 2019; Mouginot et al., 2017) to compute the nominal precision and sub-pixel matching precision of the MPIC-OPT algorithm and of the Sentinel-2 images. It consists in computing the distribution of the standard deviation values of the displacement grids per cycle length. The median of these distributions is assumed to represent the nominal precision of the sensor for each cycle length (Millan et al., 2019). The sub-pixel image matching precision is computed as  $mp = (\sigma_{cycle} * c / ps$  where  $\sigma_{cycle}$  is the standard deviation of a given cycle,  $c$  is the cycle length and  $ps$  is the pixel size).

We computed the precision for several cycles and several runs of MPIC-OPT on the Slumgullion landslide and on the Mont-Blanc glaciers. On the Slumgullion landslide we computed the displacement grids for cycle length of 0 to 1500 days representing the minimum and maximum cycle length for the Sentinel-2 archive from the end of 2015 to mid-2020. We tested the contribution of the cloud mask, the correlation threshold ( $c_{min}$ ) and the choice of the matching algorithm (MicMac vs. GeFolki). On the Mont-Blanc glaciers, we computed the displacement grids on cycle length ranging from 0 to 400 days and compared the annual displacement for hydrological years

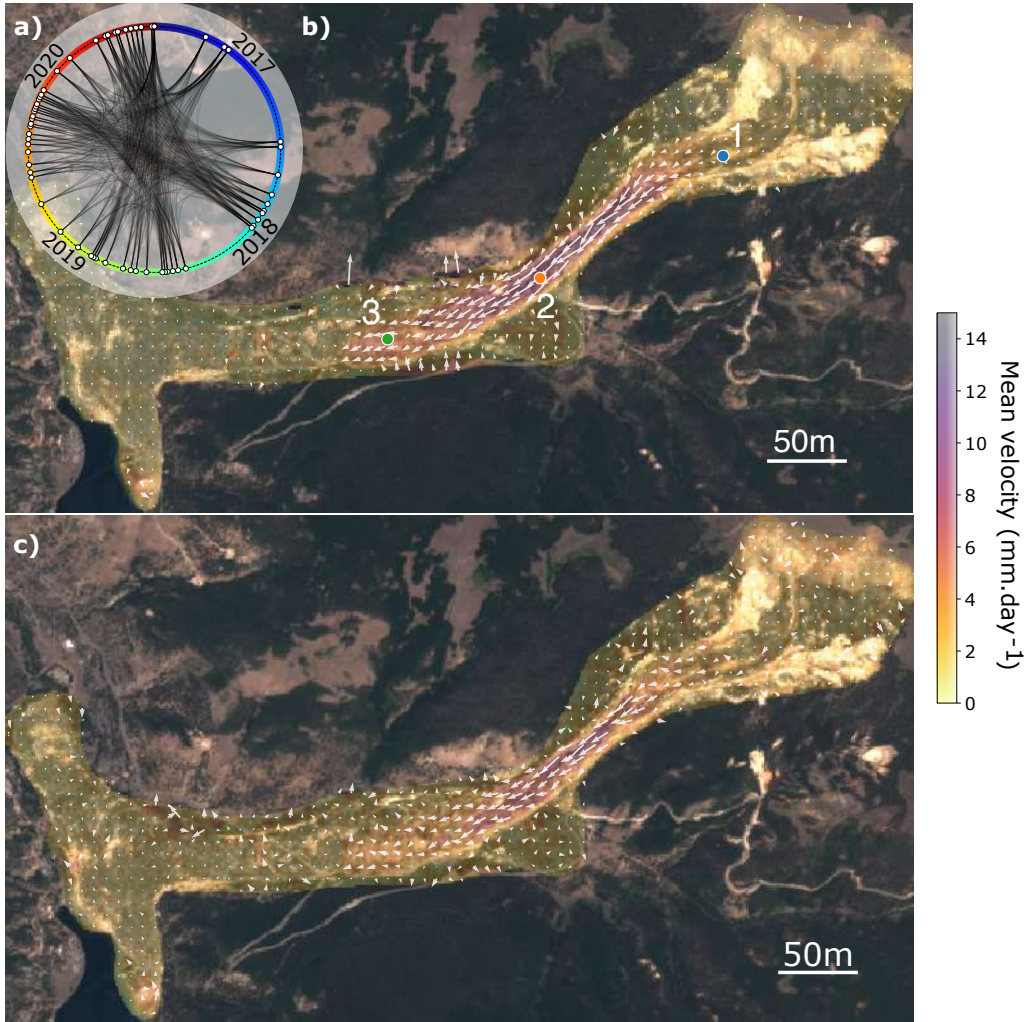


Figure 7: Results of MPIC-OPT-SLIDE on the Slumgullion landslide for the period 2015-2020. a) Chord diagram of the network of Sentinel-2 image pairs for the Slumgullion landslide; b) Mean surface velocity computed with MicMac; c) Mean surface velocity computed with GeFolki.

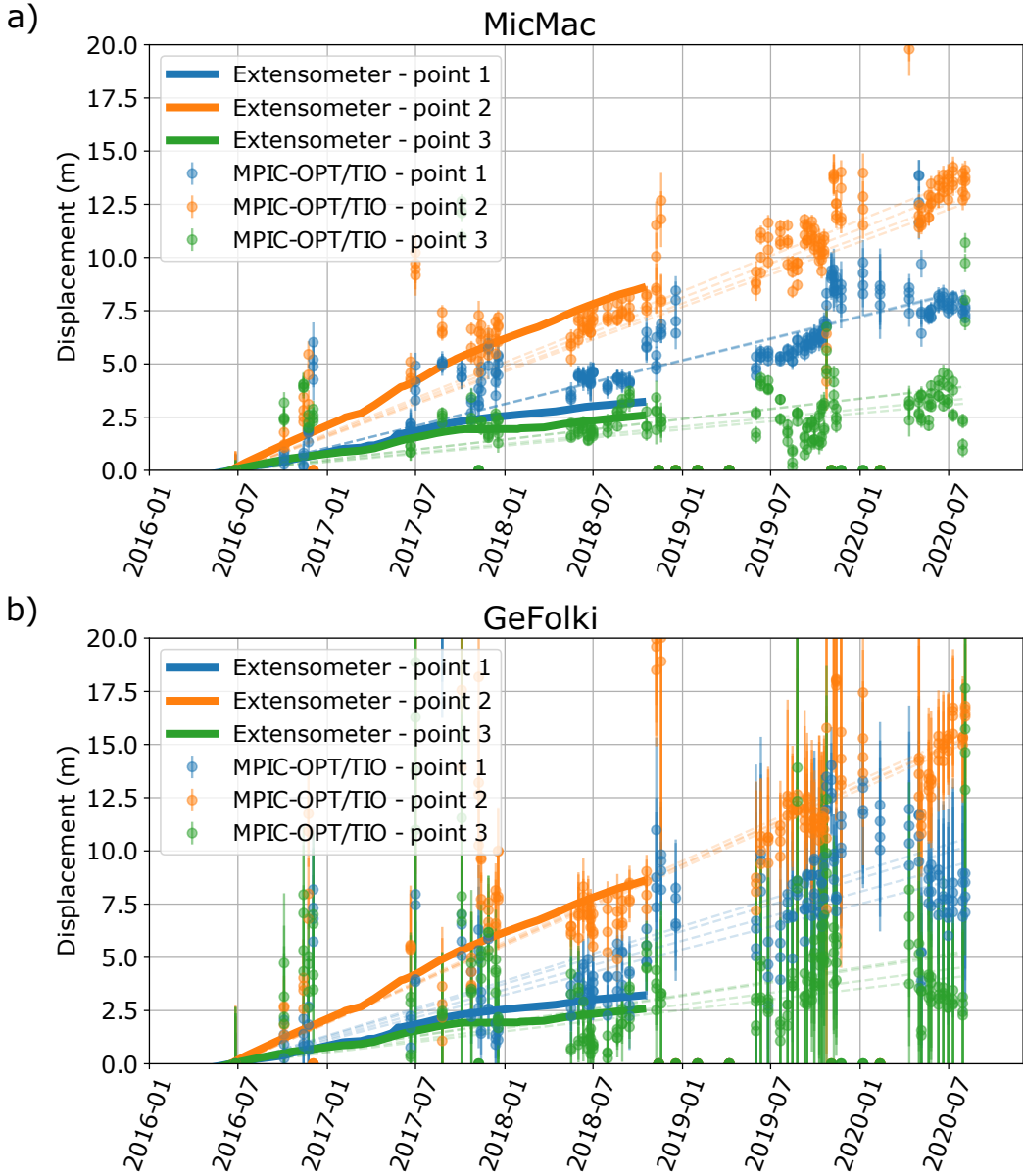


Figure 8: Comparison between the displacement time series of the three extensometers installed on the Slumgullion slope and the MPIC-OPT-SLIDE computation displacement time series provided by TIO from the inversion of the MicMac displacement grids (a) and GeFolki (b).

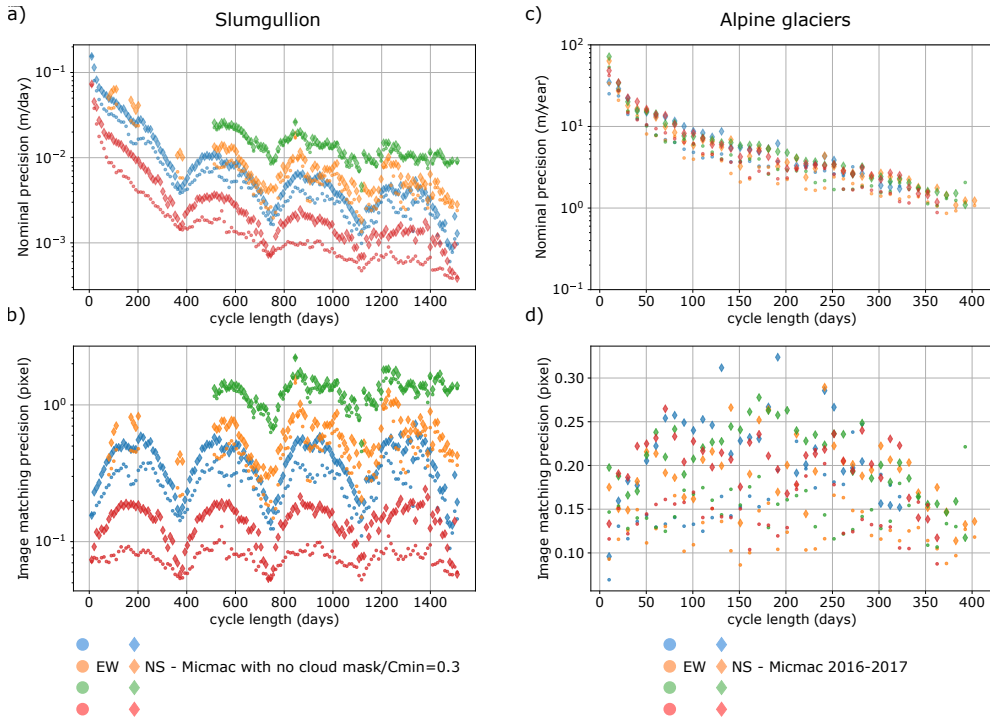


Figure 9: Mean value of the surface velocity over the Slumgullion landslide computed with GeFolki (blue arrows). To ease the comparison, the Micmac velocity vectors are displayed in white. The same set of 97 Sentinel-2 images is used with the same pairing network.

598 in order to test the stability of the precision for the Sentinel-2 archive. In  
599 both cases, we filtered out the area in motion and estimated the precision on  
600 stable zones.

601 We observe for both sites that the nominal precision decreases exponentially  
602 with the cycle length (Figure 9a, c). Second order variations are visible  
603 on both the nominal and sub-pixel matching precision (Figure 9). The pre-  
604 cision is better for yearly cycle length (i.e. 365, 730, 1095, 1460 days) and  
605 increases periodically for inter-season cycles. The precision is the lower for  
606 cycles of 182, 547, 912, 1277 days (Figure 9a, b). The amplitude of these  
607 variations for the sub-pixel precision is very large for the GeFolki algorithm  
608 ( $\Delta_{sub-pixel}^{mp} = 2.4px$ ). For the MicMac correlator, the amplitude of the vari-  
609 ations depend on the chosen parameters. The amplitudes are larger in the  
610 case of a low correlation threshold ( $c_{min} = 0.3$ ), with or without cloud mask  
611 ( $\Delta_{sub-pixel}^{mp} = 0.7px$  and  $1.9px$  respectively). They are less pronounced if the  
612 correlation threshold is larger ( $c_{min} = 0.7$ ;  $\Delta_{sub-pixel}^{mp} = 0.2px$ ). Similarly, the  
613 mean precision is very large for the GeFolki algorithm ( $\mu_{sub-pixel}^{mp} = 1.8px$ )  
614 while the MicMac runs have better sub-pixel precision ( $\mu_{sub-pixel}^{mp} = 0.5px$   
615 and  $0.8px$  with and without cloud masking respectively for  $c_{min} = 0.3$ ). The  
616 best precision is achieved with MicMac when the correlation threshold is  
617 large ( $c_{min} = 0.7$ ) with a mean precision of 0.16 pixel. We also observe that  
618 the precision of the North-South direction is systematically worse than the  
619 East-West direction (Figure 9) except for the GeFolki algorithm (Figure 9a,  
620 c in green). In particular, assuming the sensor precision is achieved with

the MicMac algorithm and a large correlation threshold, the mean sub-pixel precision of the Sentinel-2 acquisition is 0.08 pixel for the East-West direction and 0.14 for the North-South direction (Figure 9b, in red). The same observations hold for the runs on the Mont-Blanc glaciers (Figure 9c). No significant differences are observed in the displacement rates for the hydrological years over the Mont-Blanc glaciers (Figure 9c, d). For this case, the mean sub-pixel precision of the Sentinel-2 acquisition is slightly higher than the one found for the Slumgullion landslide with 0.13 pixel for the East-West direction and 0.19 pixel for the North-South direction (Figure 9d).

#### 4. Discussion

We presented the new implementation of the MPIC-OPT services that aimed at providing estimate of ground motion velocity and time series from optical image matching. The MPIC-OPT services offer a highly versatile list of functions in order to setup the best image processing strategy from the download of the images to the calculation of the correlation grids, the correction and filtering of errors, and the inversion of the time-series. Its development and implementation was thought to be tailored to the specific needs of science and operational communities expert in tectonics, landslide and glaciology while remaining flexible to be applied on various use cases. Relevant sets of parameters is proposed by default for each services in order to optimize the measure of co-seismic displacement, of ice surface velocity or landslide velocity. MPIC-OPT algorithm is proposed in several modules

in order to: 1) download and pre-process the images, 2) build the pairing network and compute the displacement grids, 3) correct and filter these displacement grids, 4) analyse the stack of displacement grids in order to compute mean velocity, detect persistent motion and/or invert the displacement time series. For each module, several parameters are open to the user for fine tuning.

#### 4.1. Influence of the jitter correction on the local deformation pattern

Nagy et al. (2019) mentioned that jitter undulations were seldom and only observed on two images over 41 images analyzed. They mentioned that no image with this effect was observed after June 2016 and the geometrical correction proposed by ESA after that date (?). The example of the Ridgecrest earthquake shows that this effect is still present in Sentinel-2 acquisitions and can drastically affect the exploitation of the Sentinel-2 acquisitions. We thus proposed a correction allowing to remove the jitter undulations observed in the displacement fields. The jitter undulations are usually removed by computing their mean amplitude over stable areas (Scherler et al., 2008) and then by removing them over the whole area. This approach poses several problems to be implemented automatically on Sentinel-2 images. First it requires the knowledge of the stable areas which is not necessarily the case; second, in the case of Sentinel-2 acquisitions, the jitter affects individually the different stripes (Figure 2a, c) making the estimation of the mean amplitude of the jitter undulations and its removal challenging even manually. The proposed

665 correction present the advantage to require no *a priori* knowledge of the sta-  
666 ble area and to perform a filtering over the whole area in a simple manner  
667 using the principle of wavelet filtering. Applying the correction improves the  
668 precision of the displacement fields by decreasing the RMSE (Figure 2) and  
669 remove significantly the number of outliers allowing a better agreement with  
670 the field observations (Figure 3,4). However, the jitter correction is sensitive  
671 to the wavelength of the deformation pattern and the choice of the wavelet  
672 family and rank determines which kind of pattern will be filtered out. In the  
673 case of the jitter undulations observed in the Sentinel-2 tile of the Ridgecrest  
674 earthquake sequence, we observed a wavelength of 1.8 - 2.0 km which is in the  
675 same order as Nagy et al. (2019). After the correction, these undulations are  
676 removed but we observed large undulations of circa 40 km (or more) result-  
677 ing in a chessboard-like pattern over the whole tile. Considering a velocity  
678 of 7 km.s<sup>-1</sup> for the satellite, these large undulations correspond to periods of  
679 5.7s (or more) per undulations. These remaining undulations are difficult to  
680 further correct adopting wavelet filtering as they are in the same wavelength  
681 as the tectonic deformation.

682 It should be noted that the proposed jitter correction is not advised when  
683 the deformation pattern of interest is of the same wavelength as the jitter  
684 undulations (circa 2 km). This explains why it is not used on the glaciers  
685 and landslides services. Also it should be noted that for tectonic deformation,  
686 the filter can remove small pattern of deformation like the one observed in  
687 the center of the NW-SE fault (Figure 10). This pattern of deformation

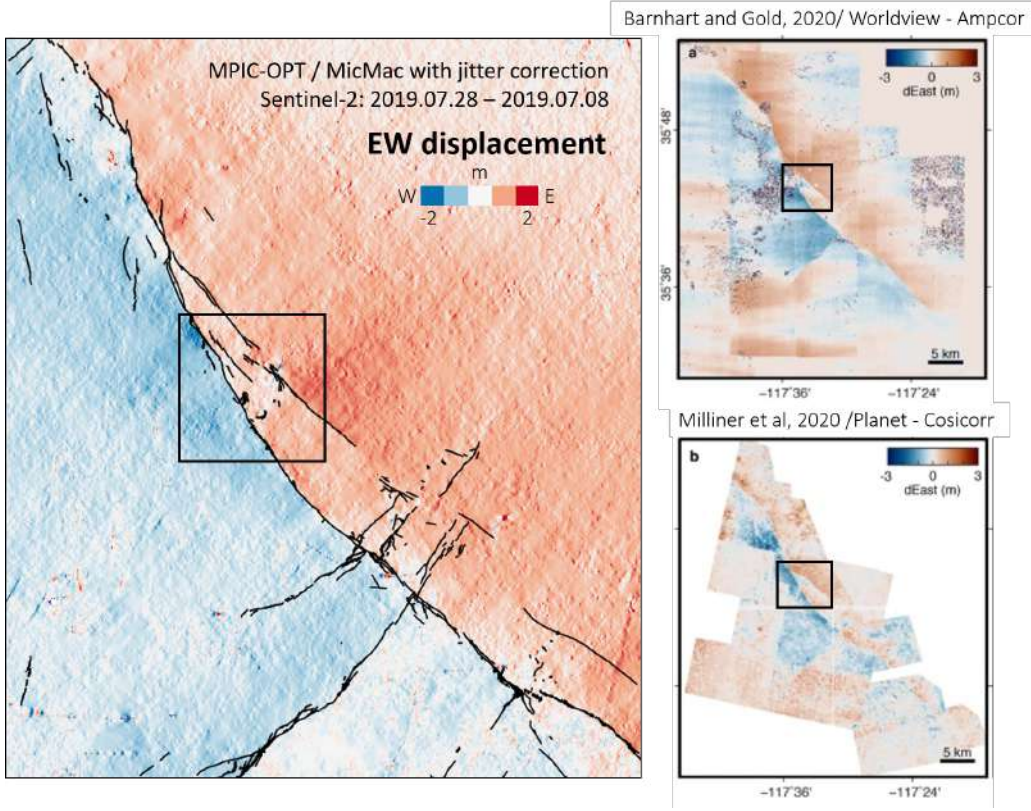


Figure 10: Effect of the MPIC-OPT-ETQ jitter correction. Left: EW displacement field computed with MPIC-OPT-ETQ with the jitter correction. Right: EW displacement fields computed with Very High Resolution images. Top: Worldview images using the Ampcorr correlator (Barnhart et al., 2019) and bottom: Planet Labsimages using the Cosi-corr correlator (Milliner and Donnellan, 2020).

688 is clearly visible on other datasets in particular with Very High Resolution  
 689 images such as Worldview (Barnhart et al., 2019) or PlanetLabs (Milliner  
 690 and Donnellan, 2020) (Figure 10). This local deformation is likely due to  
 691 superficial liquefaction and can be observed with Sentinel-2 when the jitter  
 692 correction is not applied (Chen et al., 2020).

693 *4.2. Influence of the correlation parameters and of the pairing network*

694 The accuracy of the terrain motion estimates depends on the service  
695 parameterization (Figure 9). The first obstacle to use image correlation with  
696 optical acquisitions is the presence of clouds in the images. Two strategies  
697 are tested to remove the clouds in the final results: a) classifying the pixel  
698 with Fmask to mask out the clouds before the correlation step, b) to set up a  
699 high correlation threshold (i.e.  $c_{min}$ ) to mask out pixels after the correlation.  
700 The first option is convenient to reduce the computing time and resources.  
701 However, the cloud detection algorithm tends to mask out areas not affected  
702 by clouds in particular, snow or fresh landslide outcrops. The second option  
703 presents the interest to improve significantly the quality of the results and  
704 the accuracy (Figure 9c).

A second critical parameter controlling the success of the processing is the choice of the temporal matching range to create the pairs of images. Indeed, this parameter should take into consideration the spatial resolution of the satellite ( $p$ ), the sensitivity of the matching algorithm ( $s$ ) and the minimum velocity of the studied object ( $v_{obj}$ ); therefore the minimal temporal baseline ( $\delta t$ ) should satisfy the following criteria:

$$\delta t > \frac{sp}{v_{obj}} \quad (5)$$

705 The literature reports that the accuracy of most of image correlation algo-  
706 rithm is around  $1/10^{th}$  of the pixel size (Heid and Käab, 2012; Millan et al.,

707 2019). Assuming this precision is reached, in the case of Slumgullion land-  
708 slide, cycle length of 72 days should be enough to capture the fastest part  
709 of the landslide moving at  $14 \text{ mm.day}^{-1}$  and cycle length of 300 days should  
710 capture most of the active zone. However, we show that this precision can  
711 be achieved only with a fine tuning of various parameters (Figure 9). As a  
712 consequence, it might be challenging to set up the correct cycle length to  
713 retrieve the real displacement pattern. Indeed, reducing the cycle length in  
714 case of the slow-moving object can prevent the capability of the algorithm  
715 to capture the ground motion as for example in the case of the Slumgullion  
716 landslide for cycle length of less than 300 days when the correlation thresh-  
717 old is low ( $C_{min} = 0.2$ ; Figure 11a). However, in the case of high correlation  
718 threshold ( $C_{min} = 0.7$ ), the pattern of the ground motion can be retrieved  
719 through inversion of the time series (Figure 11b) but the inverted mean ve-  
720 locity as well as the cumulative displacement show lower values (Figure 11b,  
721 c) than the ones obtained with longer cycles (Figure ??,??a). Moreover, the  
722 results with short cycle length show less agreement with in-situ observations.  
723 The choice of the temporal baseline to construct the pairing network appears  
724 to play an important role on the final results. Currently, a priori knowledge  
725 and in-situ measures seem needed to confirm the validity of the computed  
726 velocity and the displacement time series.

727 In the case of the Mont-Blanc glaciers and conversely to (Dehecq et al.,  
728 2015; Millan et al., 2019; Ali et al., 2020) we did not choose to remove the  
729 inter-seasonal pairs from our pairing network. We show that increasing the

730 correlation threshold decreases significantly the magnitude of the seasonal  
731 variations (Figure 9b) especially for the East-West component. Moreover,  
732 the inversion of the displacement time series should also help to reduce the  
733 influence of the sun illumination as demonstrated by Bontemps et al. (2018).

734 *4.3. Choice of the image matching algorithm*

735 Among the different options, the MPIC-OPT services propose two differ-  
736 ent matching algorithms: MicMac (Rupnik et al., 2017) and GeFolki (Brigot  
737 et al., 2016) based on optical flow. We test the performance of both algo-  
738 rithms on the Slumgullion landslide and show that the MicMac algorithm  
739 provides displacements grids with a better precision than GeFolki (Figure  
740 ??) as well as less noisy displacement time series (Figure ??d,e). Also, we  
741 show that the number of outliers is significantly reduced with MicMac over  
742 the Ridgecrest fault in comparison with the Cosi-Corr algorithm (Figure 3,4).  
743 These results are in line with previous studies indicating that MicMac usually  
744 provides smoother and less noisy results in comparison with other algorithms  
745 (Rosu et al., 2015; Le Bivic et al., 2017). However, one of the main advantage  
746 of GeFolki is its rapidity. Indeed, due to the pixel step-wise interpolation of  
747 the input images implemented in MicMac, the correlation computation is  
748 expensive in time and resources ( $> 1min$ , up to several minutes) while for  
749 GeFolki the resolution of the intensity equation is much faster and less ex-  
750 pensive. The GeFolki algorithm is hence a good and "cheap" alternative to  
751 obtain quick results and tune the different parameters.

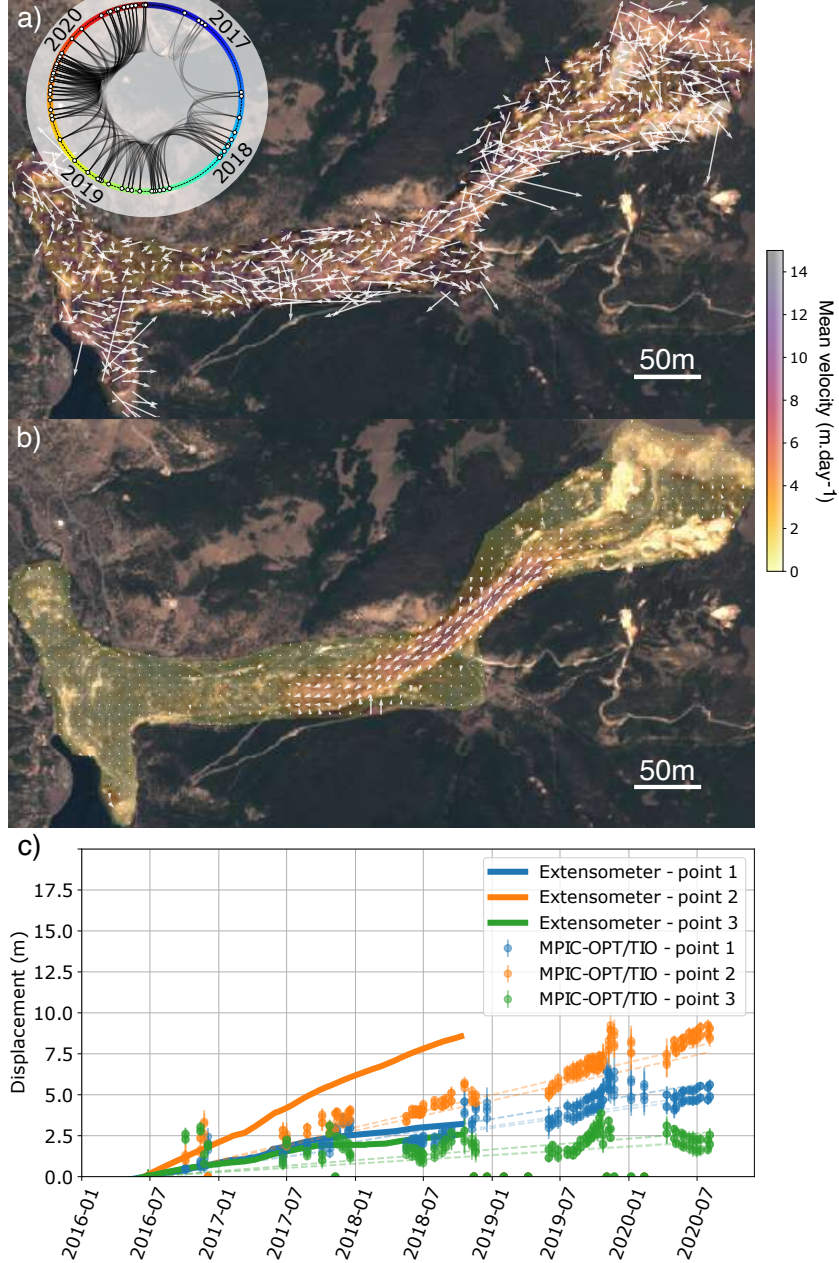


Figure 11: a) Mean surface velocity for the Slumgullion landslide from the stacking of displacement grids (MPIC) for  $c_{min} = 0.2$ , the chord diagram of the network of Sentinel-2 image pairs is plotted on the upper left corner. b) mean surface velocity obtained by linear regression of the inverted time series for  $c_{min} = 0.7$  with the same pairing network. c) inverted displacement time series at the location of the in-situ extensometers obtained from the run with  $c_{min} = 0.7$ .

752     *4.4. Optical image correlation for measuring terrain displacements*

753     Our results are in agreement with other datasets (e.g. image correlation  
754     of high resolution images over the Alps (Millan et al., 2019); UAVSAR image  
755     correlation over the Slumgullion landslide (Hu et al., 2020)) and in-situ ob-  
756     servations (Figures 8, 6). In the case of the Slumgullion landslide, we show  
757     that the exploitation of the Sentinel-2 archive provides results comparable  
758     to airborne UAVSAR dataset (Hu et al., 2020), high-resolution SAR offset  
759     tracking method using COSMO-Skymed data (Amitrano et al., 2019) and  
760     Ground-Based InSAR results (Schulz et al., 2017). Comparing to the four  
761     UAVSAR acquisition per year, the Sentinel-2 repetitive acquisition frequency  
762     provides more points of measures allowing to track seasonal variations (Fig-  
763     ure ??). Moreover, Sentinel-2 data are freely accessible while high-resolution  
764     datasets (optical or radar), UAVSAR or Ground-Based SAR acquisitions are  
765     more expensive options. Due to its ability to "see" through the clouds, SAR  
766     offset-tracking is an interesting method to retrieve high temporal resolution  
767     and was tested for glaciers (Mouginot et al., 2017; Lemos et al., 2018) and  
768     landslides (Sun et al., 2017; Amitrano et al., 2019; Dille et al., 2021) moni-  
769     toring. However, very few publications reported the use of the Sentinel-1 for  
770     landslide monitoring. The presence of vegetation and the spatial resolution  
771     of Sentinel-1 (5m x 20m) makes the application of offset tracking with this  
772     free dataset difficult for landslide monitoring but as stated by (Dille et al.,  
773     2021) probably not impossible for certain sites. The adaptation of the MPIC  
774     service to SAR acquisition is hence considered in future development.

775 We show that image matching using the Sentinel-2 archive is able to track  
776 the motion of various displacement pattern from several  $\text{mm}.\text{day}^{-1}$  to several  
777  $\text{m}.\text{day}^{-1}$  (Figure 9). Currently, the Sentinel-2 archive offers a complementary  
778 measure to InSAR results or other exploitation of the radar and optical high-  
779 resolution acquisitions (Dille et al., 2021). Exploited at a regional level,  
780 the Sentinel-2 dataset could improve the detection of active landslides as  
781 mentioned by Lacroix et al. (2018) and in a range of deformation larger than  
782 the one obtained from InSAR datasets (Rosi et al., 2018; Bekaert et al.,  
783 2020; Aslan et al., 2020). As the archive will grow with time, using image  
784 correlation may allow to access even lower displacements. This represents a  
785 potential to jointly exploit the archives of optical and radar acquisitions and  
786 retrieve the displacement in three dimensions.

787 **5. Conclusion**

788 In this work, we present the new implementation of the Multi-Pairwise  
789 Image Correlation for OPTical images algorithm (MPIC-OPT). The algo-  
790 rithm is tailored to compute ground motion from matching of optical im-  
791 ages with two matching algorithms (MicMac, GeFolki). Among the main  
792 new functions implemented, we proposed a correction for jitter undulation  
793 using a wavelet filter and we added an inversion module based on the Time-  
794 series Inversion of Optical images (TIO; Doin et al. (2011); Bontemps et al.  
795 (2018)). The algorithm is deployed on the High Performance Computing  
796 (HPC) infrastructure of the University of Strasbourg (1.5 Tier Mesocentre)

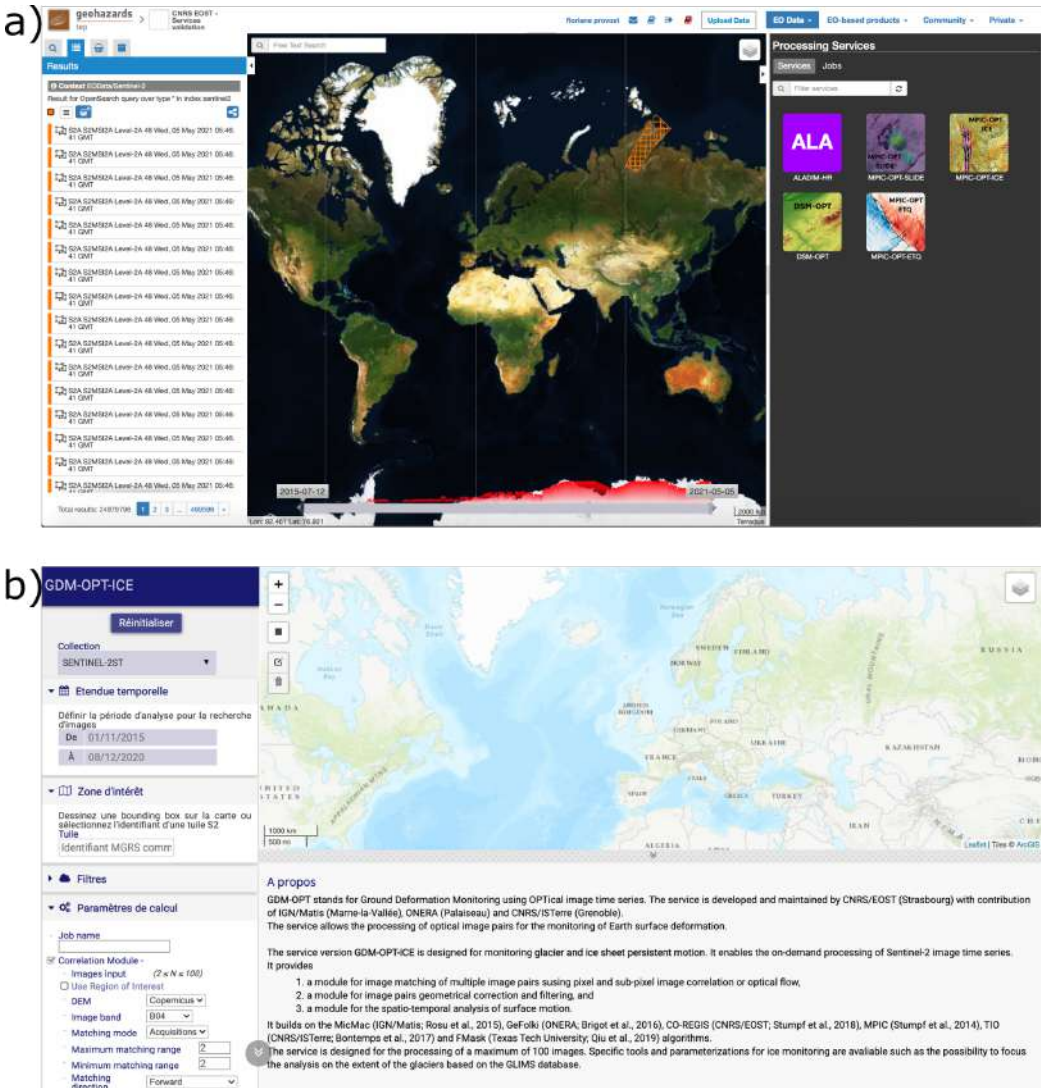


Figure 12: Screenshots of a) the Geohazards Exploitation Plateform (GEP) and b) the Form@ter webservice. Both online platforms provide access to a map, to the Sentinel catalogue and to the MPIC-OPT services.

797 allowing optimized computation, and is accessible by request through the  
798 Geohazards Exploitation Platform (GEP: [geohazards-tep.eu](http://geohazards-tep.eu); Figure 12a) or  
799 the ForM@ter webservices ([www.poleterresolide.fr](http://www.poleterresolide.fr); Figure 12b). In order to  
800 simplify the use of the services for several users community, the algorithm is  
801 accessible through three different services (ETQ, ICE, SLIDE) with, for each  
802 of them, only certain parameters open for tuning. The current version of the  
803 algorithm ingest Sentinel-2 L1C data.

804 The algorithm performances are tested on three different sites: the Ridge-  
805 crest fault, the Mont-Blanc alpine glaciers and the Slumgullion landslide.  
806 We show the ability to retrieve accurate estimation of the ground motion  
807 for regional ( $100\text{km}^2$ ) to local region of interest ( $< 1\text{km}^2$ ), for diachronic or  
808 long-term time series with several acquisitions. We tested the influence of  
809 critical parameters on the quality and precision of the terrain displacement  
810 and its ability to retrieve the displacement/velocity time series. We show  
811 that the quality of the image correlation depends on the parameters (espe-  
812 cially the correlation threshold), the choice of the algorithm and the range  
813 of the temporal baselines to create the pairing network.

814 This study demonstrates the potential of medium resolution optical im-  
815 ages (such as the Sentinel-2 acquisition) for monitoring slow to rapid hori-  
816 zontal motion and to detect motion patterns that can not be measured with  
817 other techniques (InSAR). The algorithm and its implementation on efficient  
818 computing environment provides a stable and robust service to exploit the  
819 Sentinel-2 archive and contribute to a better understanding and detection of

820 various natural hazards.

821 **6. Acknowledgements**

822 This work was financed by the European Space Agency (ESA) through the  
823 Internal Research Fellowship program and the support to the development of  
824 the Geohazards Exploitation Platform (GEP), and by the National Centre for  
825 Space Studies (CNES) part of the ForM@Ter Solid Earth data infrastructure.  
826 The authors would like to thank J. Mouginot, A. Rabatel, A. Dehecq and R.  
827 Millan (IGE, Grenoble) for their suggestions on the MPIC-OPT-ICE service,  
828 and C. Proy (CNES) for her animation of the French national working group  
829 on satellite optical data for terrain motion analysis.

830 **References**

831 , . Copernicus services coordinated interface / csci .

832 Ali, E., Xu, W., Ding, X., 2020. Improved optical image matching time  
833 series inversion approach for monitoring dune migration in north sinai  
834 sand sea: Algorithm procedure, application, and validation. ISPRS  
835 Journal of Photogrammetry and Remote Sensing 164, 106 – 124. URL:  
836 <http://www.sciencedirect.com/science/article/pii/S0924271620300952>,  
837 doi:<https://doi.org/10.1016/j.isprsjprs.2020.04.004>.

838 Altena, B., Haga, O.N., Nuth, C., Kääb, A., 2019. Monitoring sub-weekly evolution of surface velocity and elevation for a

- 840 high-latitude surging glacier using sentinel-2. ISPRS - Intern-  
841 national Archives of the Photogrammetry, Remote Sensing and  
842 Spatial Information Sciences XLII-2/W13, 1723–1727. URL:  
843 <https://www.int-arch-photogramm-remote-sens-spatial-inf-sci.net/XLII-2-W13/1723/>  
844 doi:10.5194/isprs-archives-XLII-2-W13-1723-2019.
- 845 Altena, B., Kääb, A., 2017. Weekly glacier flow estima-  
846 tion from dense satellite time series using adapted optical  
847 flow technology. Frontiers in Earth Science 5, 53. URL:  
848 <https://www.frontiersin.org/article/10.3389/feart.2017.00053>,  
849 doi:10.3389/feart.2017.00053.
- 850 Amitrano, D., Guida, R., Dell'Aglio, D., Di Martino, G., Di Martire, D.,  
851 Iodice, A., Costantini, M., Malvarosa, F., Minati, F., 2019. Long-term  
852 satellite monitoring of the slumgullion landslide using space-borne syn-  
853 synthetic aperture radar sub-pixel offset tracking. Remote Sensing 11, 369.
- 854 Aslan, G., Foumelis, M., Raucooles, D., De Michele, M., Bernardie, S., Cakir,  
855 Z., 2020. Landslide mapping and monitoring using persistent scatterer  
856 interferometry (psi) technique in the french alps. Remote Sensing 12, 1305.
- 857 Avouac, J.P., Ayoub, F., Leprince, S., Konca, O., Helmberger, D.V., 2006.  
858 The 2005, mw 7.6 kashmir earthquake: Sub-pixel correlation of aster im-  
859 ages and seismic waveforms analysis. Earth and Planetary Science Letters  
860 249, 514–528.

- 861 Ayoub, F., Leprince, S., Binet, R., Lewis, K.W., Aharonson, O., Avouac,  
862 J.P., 2008. Influence of camera distortions on satellite image registration  
863 and change detection applications, in: IGARSS 2008-2008 IEEE Interna-  
864 tional Geoscience and Remote Sensing Symposium, IEEE. pp. II–1072.
- 865 Bacques, G., de Michele, M., Foumelis, M., Raucoules, D., Lemoine, A.,  
866 Briole, P., 2020. Sentinel optical and sar data highlights multi-segment  
867 faulting during the 2018 palu-sulawesi earthquake (m w 7.5). Scientific  
868 Reports 10, 1–11.
- 869 Barnhart, W.D., Hayes, G.P., Gold, R.D., 2019. The july 2019 ridgecrest,  
870 california, earthquake sequence: Kinematics of slip and stressing in cross-  
871 fault ruptures. Geophysical Research Letters 46, 11859–11867.
- 872 Bekaert, D.P., Handwerger, A.L., Agram, P., Kirschbaum, D.B., 2020. Insar-  
873 based detection method for mapping and monitoring slow-moving land-  
874 slides in remote regions with steep and mountainous terrain: An applica-  
875 tion to nepal. Remote Sensing of Environment 249, 111983.
- 876 Bindschadler, R., Scambos, T., 1991. Satellite-image-derived velocity field of  
877 an antarctic ice stream. Science 252, 242–246.
- 878 Bontemps, N., Lacroix, P., Doin, M.P., 2018. Inversion of de-  
879 formation fields time-series from optical images, and applica-  
880 tion to the long term kinematics of slow-moving landslides in  
881 peru. Remote Sensing of Environment 210, 144 – 158. URL:

- 882        <http://www.sciencedirect.com/science/article/pii/S0034425718300282>,  
883        doi:<https://doi.org/10.1016/j.rse.2018.02.023>.
- 884        Brigot, G., Colin-Koeniguer, E., Plyer, A., Janez, F., 2016. Adaptation and  
885        evaluation of an optical flow method applied to coregistration of forest  
886        remote sensing images. IEEE Journal of Selected Topics in Applied Earth  
887        Observations and Remote Sensing 9, 2923–2939.
- 888        Brox, T., Bregler, C., Malik, J., 2009. Large displacement optical flow,  
889        in: 2009 IEEE Conference on Computer Vision and Pattern Recognition,  
890        IEEE. pp. 41–48.
- 891        Chen, K., Avouac, J.P., Aati, S., Milliner, C., Zheng, F., Shi, C., 2020.  
892        Cascading and pulse-like ruptures during the 2019 ridgecrest earthquakes  
893        in the eastern California shear zone. Nature Communications 11, 1–8.
- 894        Coe, J.A., Ellis, W.L., Godt, J.W., Savage, W.Z., Savage, J.E., Michael, J.,  
895        Kibler, J.D., Powers, P.S., Lidke, D.J., Debray, S., 2003. Seasonal move-  
896        ment of the slumgullion landslide determined from global positioning sys-  
897        tem surveys and field instrumentation, july 1998–march 2002. Engineering  
898        Geology 68, 67–101.
- 899        Cournet, M., Giros, A., Dumas, L., Delvit, J., Greslou, D., Languille, F.,  
900        Blanchet, G., May, S., Michel, J., 2016. 2d sub-pixel disparity measure-  
901        ment using qpec/medicis. International Archives of the Photogrammetry,  
902        Remote Sensing & Spatial Information Sciences 41.

- 903 Dehecq, A., Gourmelen, N., Trouve, E., 2015. Deriv-  
904 ing large-scale glacier velocities from a complete satel-  
905 lite archive: Application to the pamir–karakoram–himalaya.  
906 Remote Sensing of Environment 162, 55 – 66. URL:  
907 <http://www.sciencedirect.com/science/article/pii/S0034425715000553>,  
908 doi:<https://doi.org/10.1016/j.rse.2015.01.031>.
- 909 Delbridge, B.G., Bürgmann, R., Fielding, E., Hensley, S., Schulz, W.H.,  
910 2016. Three-dimensional surface deformation derived from airborne inter-  
911 ferometric uavstar: Application to the slumgullion landslide. Journal of  
912 geophysical research: solid earth 121, 3951–3977.
- 913 Dille, A., Kervyn, F., Handwerger, A.L., d’Oreye, N., Derauw, D., Bibentyo,  
914 T.M., Samsonov, S., Malet, J.P., Kervyn, M., Dewitte, O., 2021. When  
915 image correlation is needed: Unravelling the complex dynamics of a slow-  
916 moving landslide in the tropics with dense radar and optical time series.  
917 Remote Sensing of Environment 258, 112402.
- 918 Ding, C., Feng, G., Li, Z., Shan, X., Du, Y., Wang, H., 2016. Spatio-temporal  
919 error sources analysis and accuracy improvement in landsat 8 image ground  
920 displacement measurements. Remote Sensing 8, 937.
- 921 Doin, M.P., Guillaso, S., Jolivet, R., Lasserre, C., Lodge, F., Ducret, G.,  
922 Grandin, R., 2011. Presentation of the small baseline nsbas processing  
923 chain on a case example: the etna deformation monitoring from 2003 to

- 924        2010 using envisat data, in: Proceedings of the Fringe symposium, ESA  
925        SP-697, Frascati, Italy. pp. 3434–3437.
- 926        DuRoss, C.B., Gold, R.D., Dawson, T.E., Scharer, K.M., Kendrick, K.J.,  
927        Akciz, S.O., Angster, S.J., Bachhuber, J., Bacon, S., Bennett, S.E., et al.,  
928        2020. Surface displacement distributions for the july 2019 ridgecrest, cali-  
929        fornia, earthquake ruptures. Bulletin of the Seismological Society of Amer-  
930        ica .
- 931        Fahnestock, M., Scambos, T., Bindschadler, R., 1992. Semi-automated ice  
932        velocity determination from satellite imagery. Eos 73, 493.
- 933        Fahnestock, M., Scambos, T., Moon, T., Gardner, A., Haran, T., Klinger,  
934        M., 2016. Rapid large-area mapping of ice flow using landsat 8. Remote  
935        Sensing of Environment 185, 84–94.
- 936        Ferretti, A., Fumagalli, A., Novali, F., Prati, C., Rocca, F., Rucci, A., 2011. A  
937        new algorithm for processing interferometric data-stacks: Squeesar. IEEE  
938        transactions on geoscience and remote sensing 49, 3460–3470.
- 939        Ferretti, A., Prati, C., Rocca, F., 2001. Permanent scatterers in sar interfer-  
940        ometry. IEEE Transactions on geoscience and remote sensing 39, 8–20.
- 941        Fielding, E.J., Liu, Z., Stephenson, O.L., Zhong, M., Liang, C., Moore, A.,  
942        Yun, S.H., Simons, M., 2020. Surface deformation related to the 2019 m w  
943        7.1 and 6.4 ridgecrest earthquakes in california from gps, sar interferometry,  
944        and sar pixel offsets. Seismological Research Letters .

- 945 Fleming, R.W., (US), G.S., 1999. Map and description of the active part of  
946 the Slumgullion landslide, Hinsdale County, Colorado. US Department of  
947 the Interior, US Geological Survey.
- 948 Gascon, F., Bouzinac, C., Thépaut, O., Jung, M., Francesconi, B., Louis,  
949 J., Lonjou, V., Lafrance, B., Massera, S., Gaudel-Vacaressa, A., et al.,  
950 2017. Copernicus sentinel-2a calibration and products validation status.  
951 Remote Sensing 9, 584. URL: <http://dx.doi.org/10.3390/rs9060584>,  
952 doi:10.3390/rs9060584.
- 953 Gens, R., VAN GENDEREN, J.L., 1996. Review article sar interferom-  
954 etry—issues, techniques, applications. International Journal of Remote  
955 Sensing 17, 1803–1835.
- 956 Geudtner, D., Torres, R., Snoeijs, P., Davidson, M., Rommen, B.,  
957 2014. Sentinel-1 system capabilities and applications, in: 2014  
958 IEEE Geoscience and Remote Sensing Symposium, pp. 1457–1460.  
959 doi:10.1109/IGARSS.2014.6946711.
- 960 Guerriero, L., Di Martire, D., Calcaterra, D., Francioni, M., 2020. Digital  
961 image correlation of google earth images for earth's surface displacement  
962 estimation. Remote Sensing 12, 3518.
- 963 Heid, T., Kääb, A., 2012. Evaluation of existing image matching methods  
964 for deriving glacier surface displacements globally from optical satel-  
965 lite imagery. Remote Sensing of Environment 118, 339 – 355. URL:

- 966        <http://www.sciencedirect.com/science/article/pii/S0034425711004214>,  
967        doi:<https://doi.org/10.1016/j.rse.2011.11.024>.
- 968        Hilley, G.E., Bürgmann, R., Ferretti, A., Novali, F., Rocca, F., 2004. Dynamics  
969        of slow-moving landslides from permanent scatterer analysis. *Science*  
970        304, 1952–1955.
- 971        Hooper, A., Zebker, H., Segall, P., Kampes, B., 2004. A new method for  
972        measuring deformation on volcanoes and other natural terrains using insar  
973        persistent scatterers. *Geophysical research letters* 31.
- 974        Horn, B.K., Schunck, B.G., 1981. Determining optical flow, in: Techniques  
975        and Applications of Image Understanding, International Society for Optics  
976        and Photonics. pp. 319–331.
- 977        Hu, X., Bürgmann, R., Schulz, W.H., Fielding, E.J., 2020. Four-dimensional  
978        surface motions of the slumgullion landslide and quantification of hydrometeorological  
979        forcing. *Nature communications* 11, 1–9.
- 980        Joughin, I., Smith, B.E., Howat, I.M., Scambos, T., Moon, T., 2010. Greenland  
981        land flow variability from ice-sheet-wide velocity mapping 56, 415–430.  
982        doi:[10.3189/002214310792447734](https://doi.org/10.3189/002214310792447734).
- 983        Kääb, A., Vollmer, M., 2000. Surface geometry, thickness changes and flow  
984        fields on creeping mountain permafrost: automatic extraction by digital  
985        image analysis. *Permafrost and Periglacial Processes* 11, 315–326.

- 986 Kääb, A., Winsvold, S.H., Altena, B., Nuth, C., Nagler, T., Wuite, J., 2016.
- 987     Glacier remote sensing using sentinel-2. part i: Radiometric and geometric
- 988     performance, and application to ice velocity. *Remote Sensing* 8, 598.
- 989 Kirst, C., Skriabine, S., Vieites-Prado, A., Topilko, T., Bertin, P., Gerschen-
- 990 feld, G., Verny, F., Topilko, P., Michalski, N., Tessier-Lavigne, M., et al.,
- 991 2020. Mapping the fine-scale organization and plasticity of the brain vas-
- 992 culation. *Cell* 180, 780–795.
- 993 Konca, A.O., Leprince, S., Avouac, J.P., Helmberger, D.V., 2010. Rupture
- 994 process of the 1999 m w 7.1 duzce earthquake from joint analysis of spot,
- 995 gps, insar, strong-motion, and telesismic data: A supershear rupture with
- 996 variable rupture velocity. *Bulletin of the Seismological Society of America*
- 997 100, 267–288.
- 998 Lacroix, P., Araujo, G., Hollingsworth, J., Taipe, E., 2019. Self-entrainment
- 999 motion of a slow-moving landslide inferred from landsat-8 time series. *Jour-*
- 1000 *nal of Geophysical Research: Earth Surface* 124, 1201–1216.
- 1001 Lacroix, P., Bièvre, G., Pathier, E., Kniess, U., Jongmans, D., 2018.
- 1002 Use of sentinel-2 images for the detection of precursory motions before
- 1003 landslide failures. *Remote Sensing of Environment* 215, 507 – 516. URL:
- 1004 <http://www.sciencedirect.com/science/article/pii/S0034425718301433>,
- 1005 doi:<https://doi.org/10.1016/j.rse.2018.03.042>.
- 1006 Lauknes, T., Shanker, A.P., Dehls, J., Zebker, H., Henderson, I., Larsen, Y.,

- 1007        2010. Detailed rockslide mapping in northern norway with small baseline  
1008        and persistent scatterer interferometric sar time series methods. Remote  
1009        Sensing of Environment 114, 2097–2109.
- 1010        Le Bivic, R., Allemand, P., Quiquerez, A., Delacourt, C., 2017. Potential and  
1011        limitation of spot-5 ortho-image correlation to investigate the kinematics  
1012        of landslides: The example of “mare à poule d’eau” (réunion, france).  
1013        Remote Sensing 9. URL: <https://www.mdpi.com/2072-4292/9/2/106>,  
1014        doi:10.3390/rs9020106.
- 1015        Lemos, A., Shepherd, A., McMillan, M., Hogg, A.E., Hatton, E., Joughin, I.,  
1016        2018. Ice velocity of jakobshavn isbræ, petermann glacier, nioghalvfjerdss-  
1017        fjorden, and zachariæ isstrøm, 2015–2017, from sentinel 1-a/b sar imagery.  
1018        The Cryosphere 12, 2087–2097.
- 1019        Lenzano, M.G., Lannutti, E., Toth, C., Rivera, A., Lenzano, L., 2018. Detect-  
1020        ing glacier surface motion by optical flow. Photogrammetric Engineering  
1021        & Remote Sensing 84, 33–42.
- 1022        Leprince, S., Barbot, S., Ayoub, F., Avouac, J.P., 2007. Automatic and pre-  
1023        cise orthorectification, coregistration, and subpixel correlation of satellite  
1024        images, application to ground deformation measurements. IEEE Transac-  
1025        tions on Geoscience and Remote Sensing 45, 1529–1558.
- 1026        Leprince, S., Musé, P., Avouac, J.P., 2008. In-flight ccd distortion calibration

- 1027 for pushbroom satellites based on subpixel correlation. IEEE Transactions  
1028 on Geoscience and Remote Sensing 46, 2675–2683.
- 1029 López-Quiroz, P., Doin, M.P., Tupin, F., Briole, P., Nicolas, J.M.,  
1030 2009. Time series analysis of mexico city subsidence constrained by  
1031 radar interferometry. Journal of Applied Geophysics 69, 1 – 15. URL:  
1032 <http://www.sciencedirect.com/science/article/pii/S0926985109000251>,  
1033 doi:<https://doi.org/10.1016/j.jappgeo.2009.02.006>. advances in SAR In-  
1034 terferometry from the 2007 Fringe Workshop.
- 1035 Madson, A., Fielding, E., Sheng, Y., Cavanaugh, K., 2019. High-resolution  
1036 spaceborne, airborne and in situ landslide kinematic measurements of the  
1037 slumgullion landslide in southwest colorado. Remote Sensing 11, 265.
- 1038 Massonnet, D., Feigl, K.L., 1998. Radar interferometry and its application  
1039 to changes in the earth’s surface. Reviews of geophysics 36, 441–500.
- 1040 Massonnet, D., Rossi, M., Carmona, C., Adragna, F., Peltzer, G., Feigl,  
1041 K., Rabaute, T., 1993. The displacement field of the landers earthquake  
1042 mapped by radar interferometry. Nature 364, 138–142.
- 1043 Messerli, A., Grinsted, A., 2015. Image georectification and feature track-  
1044 ing toolbox: Imgraft. Geoscientific Instrumentation, Methods and Data  
1045 Systems 4, 23.
- 1046 Michel, R., Avouac, J.P., Taboury, J., 1999. Measuring ground displace-

- 1047 ments from sar amplitude images: Application to the landers earthquake.
- 1048 Geophysical Research Letters 26, 875–878.
- 1049 Milillo, P., Fielding, E.J., Shulz, W.H., Delbridge, B., Burgmann, R., 2014.
- 1050 Cosmo-skymed spotlight interferometry over rural areas: The slumgullion
- 1051 landslide in colorado, usa. IEEE Journal of Selected Topics in Applied
- 1052 Earth Observations and Remote Sensing 7, 2919–2926.
- 1053 Millan, R., Mouginot, J., Rabatel, A., Jeong, S., Cusicanqui, D., Derkacheva,
- 1054 A., Chekki, M., 2019. Mapping surface flow velocity of glaciers at regional
- 1055 scale using a multiple sensors approach. Remote Sensing 11, 2498. URL:
- 1056 <http://dx.doi.org/10.3390/rs11212498>, doi:10.3390/rs11212498.
- 1057 Milliner, C., Donnellan, A., 2020. Using daily observations from planet labs
- 1058 satellite imagery to separate the surface deformation between the 4 july m
- 1059 w 6.4 foreshock and 5 july m w 7.1 mainshock during the 2019 ridgecrest
- 1060 earthquake sequence. Seismological Research Letters .
- 1061 Mouginot, J., Rignot, E., Scheuchl, B., Millan, R., 2017. Comprehensive
- 1062 annual ice sheet velocity mapping using landsat-8, sentinel-1, and radarsat-
- 1063 2 data. Remote Sensing 9, 364.
- 1064 Nagy, T., Andreassen, L.M., Duller, R.A., Gonzalez, P.J.,
- 1065 2019. Sendit: The sentinel-2 displacement toolbox with
- 1066 application to glacier surface velocities. Remote Sensing

1067        11.            URL: <https://www.mdpi.com/2072-4292/11/10/1151>,  
1068        doi:10.3390/rs11101151.

1069        Qiu, S., Zhu, Z., He, B., 2019. Fmask 4.0: Improved cloud  
1070        and cloud shadow detection in landsats 4–8 and sentinel-2 im-  
1071        agery. Remote Sensing of Environment 231, 111205. URL:  
1072        <http://www.sciencedirect.com/science/article/pii/S0034425719302172>,  
1073        doi:<https://doi.org/10.1016/j.rse.2019.05.024>.

1074        Renier, N., Adams, E.L., Kirst, C., Wu, Z., Azevedo, R., Kohl, J., Autry,  
1075        A.E., Kadiri, L., Venkataraju, K.U., Zhou, Y., et al., 2016. Mapping of  
1076        brain activity by automated volume analysis of immediate early genes. Cell  
1077        165, 1789–1802.

1078        Rosi, A., Tofani, V., Tanteri, L., Stefanelli, C.T., Agostini, A., Catani, F.,  
1079        Casagli, N., 2018. The new landslide inventory of tuscany (italy) updated  
1080        with ps-insar: geomorphological features and landslide distribution. Land-  
1081        slides 15, 5–19.

1082        Ross, Z.E., Idini, B., Jia, Z., Stephenson, O.L., Zhong, M., Wang, X.,  
1083        Zhan, Z., Simons, M., Fielding, E.J., Yun, S.H., Hauksson, E., Moore,  
1084        A.W., Liu, Z., Jung, J., 2019. Hierarchical interlocked orthogonal  
1085        faulting in the 2019 ridgecrest earthquake sequence. Science 366, 346–  
1086        351. URL: <https://science.sciencemag.org/content/366/6463/346>,  
1087        doi:10.1126/science.aaz0109, arXiv:<https://science.sciencemag.org/content/366/6463/346>

- 1088 Rosu, A.M., Pierrot-Deseilligny, M., Delorme, A., Binet, R., Klinger,  
1089 Y., 2015. Measurement of ground displacement from optical satellite  
1090 image correlation using the free open-source software micmac. ISPRS  
1091 Journal of Photogrammetry and Remote Sensing 100, 48 – 59. URL:  
1092 <http://www.sciencedirect.com/science/article/pii/S0924271614000653>,  
1093 doi:<https://doi.org/10.1016/j.isprsjprs.2014.03.002>. high-Resolution Earth  
1094 Imaging for Geospatial Information.
- 1095 Rupnik, E., Daakir, M., Deseilligny, M.P., 2017. Micmac—a free, open-source  
1096 solution for photogrammetry. Open Geospatial Data, Software and Stan-  
1097 dards 2, 1–9.
- 1098 Scambos, T.A., Dutkiewicz, M.J., Wilson, J.C., Bindschadler, R.A., 1992.  
1099 Application of image cross-correlation to the measurement of glacier veloc-  
1100 ity using satellite image data. Remote sensing of environment 42, 177–186.
- 1101 Scherler, D., Leprince, S., Strecker, M.R., 2008. Glacier-surface velocities in  
1102 alpine terrain from optical satellite imagery—accuracy improvement and  
1103 quality assessment. Remote Sensing of Environment 112, 3806–3819.
- 1104 Schlögel, R., Doubre, C., Malet, J.P., Masson, F., 2015. Landslide defor-  
1105 mation monitoring with alos/palsar imagery: A d-insar geomorphological  
1106 interpretation method. Geomorphology 231, 314–330.
- 1107 Schulz, W., Coe, J., Shurtliff, B., Panosky, J., Farina, P., Ricci, P., Barsacchi,  
1108 G., 2012. Kinematics of the slumgullion landslide revealed by ground-

- 1109 based insar surveys. *Landslides and Engineered Slopes*, Protecting Society  
1110 through Improved Understanding 2, 1273–1279.
- 1111 Schulz, W.H., Coe, J.A., Ricci, P.P., Smoczyk, G.M., Shurtleff, B.L.,  
1112 Panosky, J., 2017. Landslide kinematics and their potential controls from  
1113 hourly to decadal timescales: Insights from integrating ground-based in-  
1114 sar measurements with structural maps and long-term monitoring data.  
1115 *Geomorphology* 285, 121–136.
- 1116 Schulz, W.H., McKenna, J.P., Kibler, J.D., Biavati, G., 2009. Relations be-  
1117 tween hydrology and velocity of a continuously moving landslide—evidence  
1118 of pore-pressure feedback regulating landslide motion? *Landslides* 6, 181–  
1119 190.
- 1120 Scott, C., Champenois, J., Klinger, Y., Nissen, E., Maruyama, T., Chiba,  
1121 T., Arrowsmith, R., 2019. The 2016 m7 kumamoto, japan, earthquake slip  
1122 field derived from a joint inversion of differential lidar topography, optical  
1123 correlation, and insar surface displacements. *Geophysical Research Letters*  
1124 46, 6341–6351.
- 1125 Strozzi, T., Kääb, A., Frauenfelder, R., 2004. Detecting and quantifying  
1126 mountain permafrost creep from in situ inventory, space-borne radar in-  
1127 terferometry and airborne digital photogrammetry. *International Journal*  
1128 of Remote Sensing 25, 2919–2931.
- 1129 Stumpf, A., Malet, J.P., Delacourt, C., 2017. Correlation of satellite

- 1130 image time-series for the detection and monitoring of slow-moving  
1131 landslides. *Remote Sensing of Environment* 189, 40 – 55. URL:  
1132 <http://www.sciencedirect.com/science/article/pii/S0034425716304394>,  
1133 doi:<https://doi.org/10.1016/j.rse.2016.11.007>.
- 1134 Stumpf, A., Michéa, D., Malet, J.P., 2018. Improved co-  
1135 registration of sentinel-2 and landsat-8 imagery for earth sur-  
1136 face motion measurements. *Remote Sensing* 10, 160. URL:  
1137 <http://dx.doi.org/10.3390/rs10020160>, doi:10.3390/rs10020160.
- 1138 Sun, L., Muller, J.P., Chen, J., 2017. Time series analysis of very slow land-  
1139 slides in the three gorges region through small baseline sar offset tracking.  
1140 *Remote Sensing* 9, 1314.
- 1141 Teshima, Y., Iwasaki, A., 2008. Correction of attitude fluctuation of terra  
1142 spacecraft using aster/swir imagery with parallax observation. *IEEE*  
1143 *Transactions on Geoscience and Remote Sensing* 46, 222–227.
- 1144 Vogel, C., Bauder, A., Schindler, K., 2012. Optical flow for glacier motion  
1145 estimation, in: *Proceedings of the 22nd ISPRS Congress*, Melbourne, Aus-  
1146 tralia.
- 1147 Van Wyk de Vries, M., Wickert, A.D., 2020. Glacier image velocime-  
1148 try: an open-source toolbox for easy and rapid calculation of high-  
1149 resolution glacier-velocity fields. *The Cryosphere Discussions* 2020,

- 1150        1–31. URL: <https://tc.copernicus.org/preprints/tc-2020-204/>,  
1151        doi:10.5194/tc-2020-204.
- 1152        Wang, K., Bürgmann, R., 2020. Co- and Early Postseismic Deformation Due  
1153        to the 2019 Ridgecrest Earthquake Sequence Constrained by Sentinel-  
1154        1 and COSMO-SkyMed SAR Data. Seismological Research Letters  
1155        URL: <https://doi.org/10.1785/0220190299>, doi:10.1785/0220190299,  
1156        arXiv:<https://pubs.geoscienceworld.org/srl/article-pdf/doi/10.1785/0220190299/49>
- 1157        Weinzaepfel, P., Revaud, J., Harchaoui, Z., Schmid, C., 2013. DeepFlow:  
1158        Large displacement optical flow with deep matching, in: IEEE Interna-  
1159        tional Conference on Computer Vision (ICCV), Sydney, Australia. URL:  
1160        <http://hal.inria.fr/hal-00873592>.
- 1161        Wright, T., Parsons, B., Jackson, J., Haynes, M., Fielding, E., England,  
1162        P., Clarke, P., 1999. Source parameters of the 1 october 1995 dinar  
1163        (turkey) earthquake from sar interferometry and seismic bodywave mod-  
1164        elling. Earth and Planetary Science Letters 172, 23–37.
- 1165        Wulder, M.A., White, J.C., Loveland, T.R., Woodcock, C.E., Belward, A.S.,  
1166        Cohen, W.B., Fosnight, E.A., Shaw, J., Masek, J.G., Roy, D.P., 2016.  
1167        The global landsat archive: Status, consolidation, and direction. Remote  
1168        Sensing of Environment 185, 271–283.
- 1169        Xu, X., Sandwell, D.T., Smith-Konter, B., 2020. Coseismic displacements

1170 and surface fractures from sentinel-1 insar: 2019 ridgecrest earthquakes.

1171 Seismological Research Letters .

1172 Yamazaki, D., Ikeshima, D., Tawatari, R., Yamaguchi, T., O'Loughlin, F.,

1173 Neal, J.C., Sampson, C.C., Kanae, S., Bates, P.D., 2017. A high-accuracy

1174 map of global terrain elevations. Geophysical Research Letters 44, 5844–

1175 5853.

1176 Ye, Z., Xu, Y., Tong, X., Zheng, S., Zhang, H., Xie, H., Stilla, U., 2019.

1177 Estimation and analysis of along-track attitude jitter of ziyuan-3 satellite

1178 based on relative residuals of tri-band multispectral imagery. ISPRS

1179 Journal of Photogrammetry and Remote Sensing 158, 188 – 200. URL:

1180 <http://www.sciencedirect.com/science/article/pii/S0924271619302497>,

1181 doi:<https://doi.org/10.1016/j.isprsjprs.2019.10.012>.